**Master's Thesis**
on

# Implementation of two-stage frequency up-conversion technique for controlling superconducting qubits

by,

**P181211 Gaurav Agarwal,**
Centre for Excellence in Basic Sciences, Mumbai

Under the guidance of,

**Prof. Rajamani Vijayaraghavan,**
Tata Institute of Fundamental Research, Mumbai


Department of Physical Sciences,
Centre for Excellence in Basic Sciences,
Mumbai, India - 400098


Department of Condensed Matter Physics,
Tata Institute of Fundamental Research,
Mumbai, India - 400005

Semester IX
2023


# Certificate

This is to certify that CEBS student **Mr. Gaurav Agarwal** has undertaken research project work under the guidance of **Prof. Rajamani Vijayaraghavan**, Tata Institute of Fundamental Research, Mumbai starting June, 2022 to December, 2022. This submitted project report titled **'Implementation of two-stage frequency up-conversion technique for controlling superconducting qubits'** is towards the academic requirements of the M.Sc. thesis at UM-DAE CEBS.

**Gaurav Agarwal**

**Dr. Rajamani Vijayaraghavan**
Research advisor
Associate Professor,
Department of Condensed Matter Physics and Material Science,
Tata Institute of Fundamental Research, Mumbai.

# Acknowledgements

"The people that you work with are, when you get down to it, your very best friends." - Michael Scott, The Office S07E21

Even a fragment of this work would not have been possible without the people in the QuMaC lab. I thank Prof. Vijayaraghavan for his constant guidance, patience, and encouragement. His insights and ability to pinpoint a problem like it is the elephant in the room have been very inspiring. I have learned new things in every interaction with him. I want to thank Jay Deshmukh for being a fantastic friend. Having learned from him experimental methods, physics, music, and, most of all, critical thinking, I thank him for his patience and mentorship. I revere his ability to convey complex concepts and his quick wit.

I would also like to thank Kishor for his guidance and numerous explanations and Dr. Sumeru for offering thoughtful input and actionable advice. I also thank Dr. Madhavi, Srijita, Anirban, Gaurav, Meghan, Lakshay, Panya, and Eeshita. Meeting up every day for coffee and lunch has been a highlight, and without them, the QuMaC lab would not have been the same.

I am forever grateful to my family for their unwavering support throughout every aspect of my life. I couldn't have achieved anything without their love and encouragement.

Gaurav Agarwal

January, 2023
UM-DAE-CBS, Mumbai

**Abstract**

Superconducting qubits have emerged as one of the front-runners in the development of quantum processors and require amplitude and phase modulated microwave frequency pulses for control and measurement. A common method for generating these pulses is the single side band up-conversion scheme which utilizes an IQ Mixer and two modulating signals from arbitrary waveform generators. In this thesis, we discuss an alternative scheme, referred to as double frequency up-conversion, which aims to reduce the number of required modulating signals to one, eschews periodic calibrations and accommodates a wider range of qubit frequencies. We partially implement this scheme, demonstrate the measurement and analysis of a single qubit, and present evidence that the long-term stability of the alternative scheme is comparable to that of the standard setup.

# Contents

# Chapter 1

# Introduction

*Quantum computing* is a field that utilizes the phenomena only allowed by quantum mechanics - superposition and entanglement - to perform operations on data. These properties effectively allow us to traverse the entire computational state simultaneously while being correlated and conditional on each other. A Quantum bit or a qubit is the fundamental building block of a quantum computer. It can be mathematically represented as a normalized state in a 2-D Hilbert space over a field of complex numbers. For a qubit in state $|\psi\rangle$ : $|\psi\rangle = a\,|0\rangle + b\,|1\rangle$, where $a, b \in \mathbb{C}$ and $\sqrt{|a|^2 + |b|^2} = 1$.

Qubits require true quantum systems that can be probed, manipulated and their interaction with each other controlled. Qubits have been implemented in several ways, including optical lattices, ion traps, Nuclear Magnetic Resonance, semiconductor traps for electrons, diamond NV centers, and superconducting circuits [1]. However, all these implementations have been plagued by the loss of quantum information with time, called decoherence which is caused due to noise introduced by the interaction of these quantum systems with the environment. Practical quantum computation can only be achieved when decoherence times are pushed further, gates made faster, and the number of qubits scaled higher. The field is faced with engineering challenges and open problems, making it an exciting and active field to pursue.

A major front-runner in the field has been superconducting circuits in a cQED architecture. The platform offers coherence times exceeding $100\mu s$, fast quantum gates in the order of a few tens of nanoseconds, and artificial engineering of Hamiltonians [2]. In this thesis, we present superconducting circuits as our platform and explore a double-frequency up-conversion scheme to implement qubit control while optimizing RF components.

## 1.1 The field of superconducting circuits

Superconductivity is a macroscopic phenomenon where paired electrons - or cooper pairs - condense into one state. It offers a dissipation-free environment for electrons and, therefore, can serve as a basis for our system. Resonant electrical circuits with inductors and capacitors can be readily fabricated with superconductors. The energy of an LC oscillator can be written as:

$$\mathcal{H} = \frac{Q^2}{2C} + \frac{\phi^2}{2L} \tag{1.1}$$

where $Q$ is the charge in the capacitor and $\phi$ is the flux in the inductor. These can be treated as canonical momentum and position variables respectively as shown below:

$$\begin{aligned} \frac{\partial \mathcal{H}}{\partial Q} &= \frac{Q}{C} = V = -L\frac{\partial I}{\partial t} = -\dot{\phi} \\ \frac{\partial \mathcal{H}}{\partial \phi} &= \frac{\phi}{L} = I = \dot{Q} \end{aligned} \tag{1.2}$$

Further, we can extend the canonical variables to their quantum mechanical counterparts, $\hat{Q}$ and $\hat{\phi}$, such that $[\hat{Q}, \hat{\phi}] = -i\hbar$. The Hamiltonian now becomes quantized [2],

$$\hat{\mathcal{H}} = \frac{\hat{Q}^2}{2C} + \frac{\hat{\phi}^2}{2L} = \hbar\omega_0(\hat{a}^\dagger\hat{a} + \frac{1}{2})) \tag{1.3}$$

where $\hat{a}^\dagger, \hat{a}$ are standard ladder operators, $\omega_0 = 1/\sqrt{LC}$ is the standard resonant frequency of the oscillator.

## 1.2 Josephson Junction

The elements introduced above form quantum harmonic oscillators. Therefore, accessing a particular energy level for encoding computational bits is impossible. A dissipation-less non-linear element called the Josephson Junction - a junction of superconductor-insulator-superconductor - solves the problem and forms the heart of superconducting circuits. The super-current across the Josephson Junction (JJ) can be written as [3].

$$I(t) = I_c \sin\left(\frac{2\pi\Phi(t)}{\Phi_0}\right) = I_c \sin(\phi(t)) \tag{1.4}$$

where $\Phi(t)$ is the phase difference of the Ginzberg-Landau order parameter (wave-function) in the two superconductors and $\Phi_0 = h/2e$ is the flux quantum. The

phase difference evolves with voltage as

$$\hbar \frac{d\phi}{dt} = 2eV \tag{1.5}$$

On comparison with $V = -L\dot{I}$, we can identify the associated inductance as

$$L_J = \frac{\hbar}{2eI_c \cos(\phi)} = \frac{L_J 0}{\sqrt{1 - (I/I_c)^2}} \tag{1.6}$$

The energy stored in this inductor can be calculated by integrating the power from $\phi = 0$ to $\phi = \delta$ to get

$$U = \frac{I_c \Phi_0}{2\pi} \int_0^\delta \sin(\delta) d\delta = E_J(1 - \cos\delta) \tag{1.7}$$

which serves as the source of an anharmonic potential. Armed with this element, we can construct our qubits.

## 1.3 Transmon Qubit

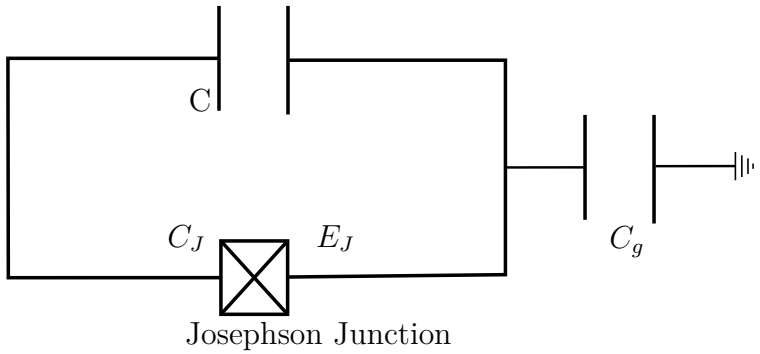


Figure 1.1: Construction of the transmon qubit. The symbol for Josephson junction is also shown.

Replacing the inductor in an LC oscillator with a Jospehson Junction gives us

$$\hat{\mathcal{H}} = \frac{\hat{Q}^2}{2C} + E_J[1 - \cos\hat{\delta}]. \tag{1.8}$$

where $E_J = \hbar I_0/2\pi$. Defining $n = Q/2e$ as the number of Cooper pairs with charging energy $E_C = e^2/(2C)$ where $C$ is the total capacitance across the junction,

we can write the above in terms of charge units 'n'. The Hamiltonian transforms to [4],

$$\hat{\mathcal{H}} = 4E_C(\hat{n} - \hat{n_g})^2 - E_J \cos\hat{\delta} \tag{1.9}$$

where $n_g$ represents the offset charge due to stray coupling. This term makes the system susceptible to charge noise, as any fluctuation in $n_g$ will change the system's eigenvalues. In the limit, $E_J/E_C \gg 1$ (i.e., $\delta \ll 1$), the energy becomes insensitive to charge noise [5]. This is called the transmon regime. The analytical solution in $\delta$-basis to (1.9) is in terms of Matthieu functions; however, under the approximation $\delta \ll 1$, we may expand the cosine up to the fourth order and quantize the Hamiltonian to get [4]:

$$\hat{H}_{\text{trans}} = \omega_{01} b^\dagger b + \frac{\alpha}{2} b^\dagger b^\dagger b b \tag{1.10}$$

The spectrum contains several energy eigenstates; however, we will only use the first level, $\omega_{01}$, to define the computational sub-space for our qubit. We define the anharmonicity $\alpha = (\omega_{12} - \omega_{01})$. This difference must be large enough to drive $\omega_{01}$ without exciting any other state. Optimally controlling these parameters results in the transmon qubit. For the transmon, anharmonicity $\alpha = -E_C$ (under the approximation $E_J/E_C \gg 1$ ) is generally designed to be between $100 - 300$MHz, $\omega_{01} \simeq 3 - 6$GHz and $E_J/E_C > 50$ [2]. Therefore, we can consider our transmon qubit to be a two-level system, defined as

$$\hat{H}_q = -\frac{\omega_q}{2}\sigma_z \tag{1.11}$$

## 1.4 Cavity Quantum Electrodynamics

The qubit has to be controlled and probed. This is achieved by placing the qubit in a cavity that supports a discrete set of modes ($m$). The electric and magnetic fields in these modes can be thought of as canonical position and momentum variables, respectively. Each mode is orthogonal and acts as an individual harmonic oscillator and can be quantized as in section (1.1). The Hamiltonian for mode $m$ can be represented as:

$$\hat{H}_m |n\rangle = E_n^m |n\rangle, \qquad E_n^m = \omega_c(n + \frac{1}{2})$$

where $|n\rangle$ are the Fock states. We will restrict ourselves to the lowest mode ($m = 1$) of the cavity. The qubit interacts via its dipole moment with the electric field in this mode with the Hamiltonian:

$$H_{int} = -\hat{E}(t) \cdot \hat{d}_{\|} = -g\left(\hat{a} + \hat{a}^\dagger\right)(\sigma_+ + \sigma_-),$$

where $\hat{d}_{\|}$ is the component dipole moment of the qubit aligned with the electric field of the cavity, $\sigma_{+,-}$ are the raising and lowering operators of the qubit and $\{a^\dagger, a\}$ are the creation and annihilation operators of the cavity.

## 1.5 Jaynes-Cummings Model

The Hamiltonians of the qubit and cavity discussed in the previous sections can be combined to represent the qubit-cavity system as [6],

$$\mathcal{H}_{\mathcal{JC}} = \omega_c \left(\hat{a}^\dagger \hat{a} + \frac{1}{2}\right) - \frac{1}{2}\omega_q \sigma_z - g\left(\hat{a} + \hat{a}^\dagger\right)(\sigma_+ + \sigma_-) \tag{1.12}$$

where the first term represents the cavity, the second term represents the qubit, and the third term represents the interaction between the qubit and the cavity. We can simplify this Hamiltonian by a rotating wave approximation under the assumption that the coupling strength $g \ll \omega_q, \omega_c$ [1]. The interaction term has four sub-terms:

$$H_{int} = \hat{a}^\dagger \sigma_- + \hat{a}\sigma_+ + \hat{a}^\dagger \sigma_+ + \hat{a}\sigma_-$$

The last two terms have higher energy ($\pm(\omega_c + \omega_q)$), and therefore happen on a much faster timescale that the first two processes and average out to zero on the timescales of the first two processes [4]. With this approximation, we arrive at the Jaynes-Cummings Hamiltonian:

$$\mathcal{H}_{\mathcal{JC}} = \omega_c \left(\hat{a}^\dagger \hat{a} + \frac{1}{2}\right) - \frac{1}{2}\omega_q \sigma_z - g\left(\hat{a}^\dagger \sigma_- + \hat{a}\sigma_+\right) \tag{1.13}$$

The Hamiltonian exists in an $\infty$-D Hilbert space, and has a block-diagonal form in the bare basis state:

$$H_{JC} = \begin{pmatrix} \frac{1}{2}\omega_c - \frac{\omega_q}{2} & 0 & 0 & 0 & 0 & 0 \\ 0 & \frac{3}{2}\omega_c - \frac{\omega_q}{2} & g & 0 & 0 & 0 \\ 0 & g & \frac{3}{2}\omega_c + \frac{\omega_q}{2} & 0 & 0 & 0 \\ & & & \cdots & & \\ 0 & 0 & 0 & 0 & \left(n+\frac{1}{2}\right)\omega_c - \frac{\omega_q}{2} & \sqrt{n+1}g \\ 0 & 0 & 0 & 0 & \sqrt{n+1}g & \left(n+\frac{1}{2}\right)\omega_c + \frac{\omega_q}{2} \end{pmatrix},$$

All blocks follow a general form (except the first block). Each block (say $M_n$) can be individually diagonalized:

$$M_n = \begin{pmatrix} \left(n+\frac{1}{2}\right)\omega_c - \frac{\omega_q}{2} & \sqrt{n+1}g \\ \sqrt{n+1}g & \left(n+\frac{1}{2}\right)\omega_c + \frac{\omega_q}{2} \end{pmatrix},$$

[1] $g$ represents the coupling of the $0 \to 1$ transition to the cavity in this case, however, this analysis can also be done including other transition effects.

The eigenvalues to the system come out to be [4],

$$\begin{aligned} E_g &= -\frac{\Delta}{2} \\ E\mp &= (n+1)\omega_c \mp \frac{1}{2}\sqrt{4g^2(n+1)+\Delta^2} \end{aligned} \tag{1.14}$$

where $\Delta = \omega_q - \omega_c$. When $n = 0$,

$$E_\mp - E_g = \omega_c \mp \frac{1}{2}\sqrt{4g^2+\Delta^2} + \Delta/2 \tag{1.15}$$

which displays the phenomena of avoided crossing [2]. This difference between the levels is significant when $\Delta/g \gg 1$. Therefore, under this design, we can construct our two-level system. This approximation is called the dispersive approximation and is interpreted as the cavity and qubit being far detuned.

Under the dispersive regime, the interaction term in the Hamiltonian is relatively weak. Therefore, we consider the unitary transformation $\hat{U} = e^{\lambda(\sigma - a^\dagger - \sigma + a)}$ on the Hamiltonian to transform to a rotating frame,

$$\hat{U}\hat{H_{JC}}\hat{U}^\dagger = \omega_c\left(\hat{a}^\dagger\hat{a} + \frac{1}{2}\right) - \frac{1}{2}\omega_q\sigma_z - \frac{g^2}{\Delta}\hat{a}^\dagger\hat{a}\sigma_z + \frac{g^2}{2\Delta}\sigma_z \tag{1.16}$$

We can absorb the constant lamb shift term into $\omega_q$ term and get:

$$\hat{H_{dis}} = \omega_c\hat{a}^\dagger\hat{a} - \frac{1}{2}\omega_q\sigma_z - \frac{g^2}{\Delta}\hat{a}^\dagger\hat{a}\sigma_z \tag{1.17}$$

where the first term is the cavity term, second term is the qubit, and the third term is the coupling term between the qubit and the cavity. We can rearrange this to be:

$$\hat{H_{dis}} = (\omega_c - \chi\sigma_z)\hat{a}^\dagger\hat{a} - \frac{1}{2}\omega_q\sigma_z \tag{1.18}$$

where $\chi = g^2/\Delta$. However this value is specifically for a two level system. For a weakly anharmonic oscillator coupled to a harmonic oscillator, it is important to consider higher levels. On including the effects of three higher levels the dispersive shift changes to [9]

$$\chi = \frac{g^2}{\Delta}\left(\frac{\alpha}{\Delta - \alpha}\right) \tag{1.19}$$

We can observe that the cavity frequency depends on the qubit's state. Therefore we can detect the change in the cavity's resonant frequency for measuring the state of the qubit.

## 1.6 Dynamics of a qubit

Controlling the state of the qubit requires driving the qubit with an electric field. While we can treat our drive as a coherent state of light, we use a semi-classical model for simplicity and an intuitive understanding of the physics. The qubit interacts with the electric field with its inherent dipole moment. The Hamiltonian can be written as:

$$H = \frac{1}{2}\omega_q\sigma_z - E(t).\hat{d}_{\|} = \frac{1}{2}\omega_q\sigma_z - A\cos\omega_d t\sigma_x$$

where $A = Ed$. Since there are two frequencies, we can go into a rotating frame as done in the section before. Consider the unitary operator, $U(t) = \exp\{-i\frac{\omega_d}{2}\sigma_z t\}$. Under the transformation

$$\hat{\mathcal{H}} = U(t)\hat{H}U^{\dagger}(t) - i\dot{U}^{\dagger}(t)$$

the Hamiltonian becomes:

$$\hat{\mathcal{H}} = -\frac{1}{2}\Delta_d\sigma_z - \frac{E_d}{2}\sigma_x$$

which is time independent. We can diagonalize this Hamiltonian in the qubit energy basis to get

$$E_{\pm} = \pm\frac{1}{2}\sqrt{A^2 + \Delta_d^2}$$

and eigenstates,

$$|V_-\rangle = \cos(\theta)|e\rangle - \sin(\theta)|g\rangle,$$
$$|V_+\rangle = \sin(\theta))|e\rangle + \cos(\theta)|g\rangle$$

where $\theta = \tan^{-1}\left(\frac{A}{\sqrt{A^2+\Delta_d^2}-\Delta_d}\right)$. The state then becomes

$$|\psi(t)\rangle = C_+e^{-iE_+t}|V_+\rangle + C_-e^{-iE_-t}|V_-\rangle$$

where $C_{\pm}$ are the initial conditions of the qubit. Taking $|\psi(0)\rangle = |g\rangle$, we have $C_+ = \cos(\theta)$ and $C_- = -sin(\theta)$. Writing the above in terms of the qubit states, we get

$$|\psi(t)\rangle = -i\sin(E_+t)\sin(2\theta)|e\rangle + \cos(E_+t)\sin(2\theta)|g\rangle \tag{1.20}$$

The expectation value of being in the excited state is simply,

$$P_e(t) = \sin^2(2\theta)\sin^2(E_+t) = \frac{A^2}{A^2+\Delta_d^2}\sin^2\left(\frac{\sqrt{A^2+\Delta_d^2}}{2}t\right) \tag{1.21}$$

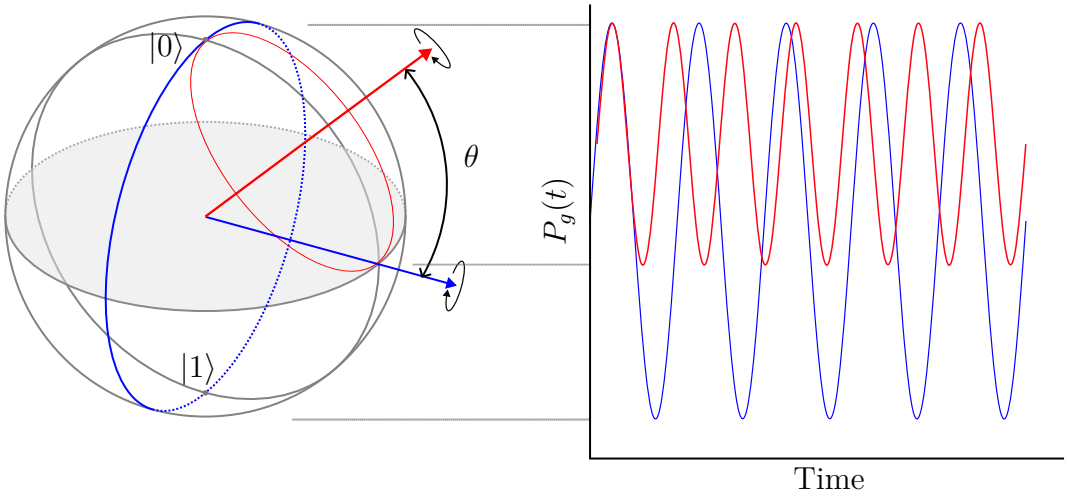


Figure 1.2: The effect of a coherent drive on the two level system depicted on a Bloch Sphere. The schematic is made with respect to the rotating frame of the qubit.

Therefore, under a coherent drive, we observe oscillations of the qubit state between $|g\rangle$ and $|e\rangle$. These are called Rabi oscillations. The schematic (1.2) shows the effect of detuning on the oscillations.
Once a qubit is driven with a specific phase $\phi_o$, all drives following it must be phase shifted with time with respect to $\phi_o$. Changing the phase to $\phi_o + \pi/2$ essentially changes the axis of rotation on the Bloch sphere. Rotations around the x-axis are termed $X$ rotations, i.e., a $180^o$ rotation about the X-axis would be a $X_\pi$ rotation. (refer figure (1.3) ).

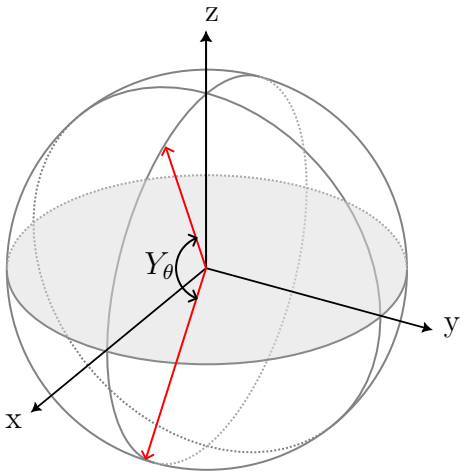


Figure 1.3: Rotations of an angle $\theta$ about the y-axis are simply termed $Y_\theta$ rotations.

Under experimental conditions, no system is isolated. The system eventually ex-

changes energy, and the system's quantum properties degrade, which is called decoherence. While modeling of this is extensively done in the emerging field of quantum thermodynamics, in this thesis, we will limit ourselves to the phenomenological picture of dissipation dynamics:

- **Relaxation**: A qubit in a cavity is shielded from environmental noise. However, it is still indirectly coupled to the outside environment through the cavity. Imperfections in the cavity or the qubit introduce decay channels. A qubit in excited state $|e\rangle$ eventually decays to $|g\rangle$ at a random time. Therefore, as soon as the qubit is prepared in an excited state, the probabilities of being excited or in ground state must evolve. We characterise the time scale where the qubit spontaneously relaxes as $T_1$, called the relaxation time, and the probability of the qubit being excited is modeled by $P_e(t) = P_e(0)e^{-t/T_1}$.

- **Dephasing** : Due to various imperfections and noises in the system, the frequency of the qubit may shift. This effectively translates into a noise in the phase of the qubit wavefunction. The uncertainty of the phase grows with time and is characterized by $T_\phi$, called the dephasing time. The transverse relaxation time $T_2$ can be calculated as $1/T_2 = 1/(2T_1) + 1/T_\phi$.

Both the above need to be characterized for a given qubit and serve as threshold limits above which extracted dynamics from the qubit cannot be trusted.

## 1.7 RF Control

The resonant frequency of the transmon, as discussed in section (1.1), lies in the microwave regime. Therefore, generation and modulation of microwave pulses with precise amplitude, phase and frequency is required. For this purpose, we use a combination of multiple RF components like mixers, amplifiers and filters. Some of the schemes and their requirements follow:

### 1.7.1 Three port mixer

As the name suggests, a three port mixer is a three-port device [7] that uses a non-linear element (diode/transistor) to generate the sum and difference of the frequencies of two input signals as shown in schematic (1.4).

The ports are named the LO port, the IF port, and the RF output port. The IF or the intermediate frequency port is typically a low-frequency port and can be used as both an input and an output (as shown in 2.3). The LO or Local Oscillator port is usually driven with a continuous sinusoidal wave. The LO signal is used to power the mixer and is only used as an input port.

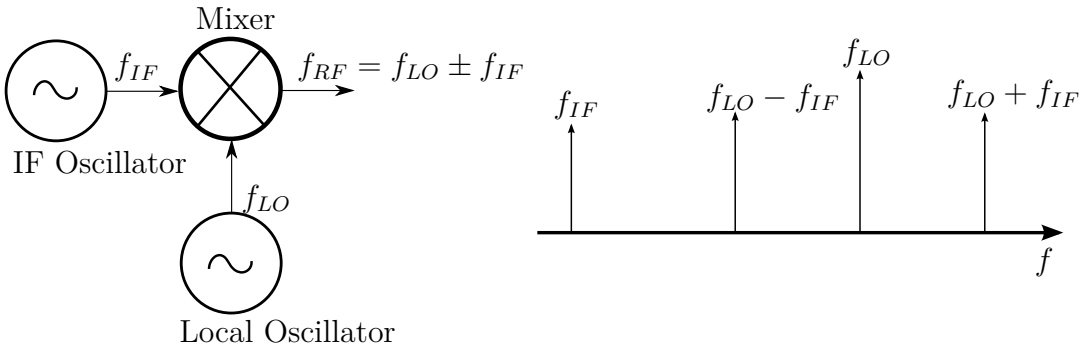


Figure 1.4: The symbol of a mixer is shown. The LO and IF frequencies combine to get the output of the sum and difference of their frequencies.

The mathematical operation a mixer represents is:

$$\begin{aligned} V_{RF} =& KV_{IF} \times V_{LO} \\ =& K\cos(\omega_{IF}t)\cos(\omega_{LO}) \\ =& \frac{K}{2}(\cos((\omega_{LO}-\omega_{IF})t) + \cos((\omega_{LO}+\omega_{IF})t)) \end{aligned} \tag{1.22}$$

where K is a constant that accounts for conversion losses.

### 1.7.2 IQ Mixer

An IQ mixer is a four-port mixer with two IF inputs, an LO input and an RF output. Schematic (1.5) shows the construction of the mixer and it uses two three-port mixers along with a 90 degree hybrid and a power combiner.

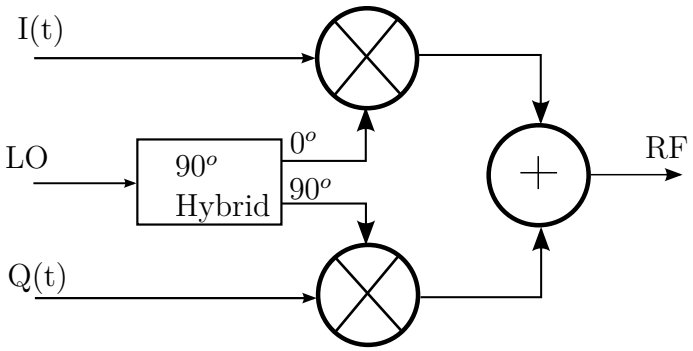


Figure 1.5: Schematic of an IQ mixer. The LO is phase shifted[7] using a hybrid by $90^o$ and fed into two separate mixers, where they mix with the quadratures $I(t)$ & $Q(t)$ and combine into one transmission line.

The operation that an IQ mixer renders, considering $V_{LO} = \cos(\omega_{LO}t)$, is:

$$V_{RF} = I(t) \times \cos(\omega_{LO}t) + Q(t) \times \sin(\omega_{LO}t) \tag{1.23}$$

The advantage of the IQ mixer lies herein. By controlling the two quadratures, we can adjust the amplitude and phase of the RF signal in real-time. This mixer can also act as a gate, i.e. if $I(t) = Q(t) = 0$, $V_{RF}$ would be zero.

### 1.7.3 Non-idealities of a mixer

In an ideal mixer, it is assumed that the two branches depicted in figure (1.5) are identical both in amplitude and in phase. However, practically, it is rarely the case. Except conversion losses, there are two main non-idealities that we need to account for.

- The $90^0$ hybrid used to phase shift LO may not be accurate. The hybrid entirely depends on path lengths which can change with deviations in temperature and the operating frequency [7]. This can be compensated for by adjusting the phase difference in $I(t)$ and $Q(t)$ accordingly.
- There is an LO leakage at the RF port even when $I(t) = Q(t) = 0$. We can adjust this by adding DC offsets to $I(t)$ and $Q(t)$.

Moreover, there can also be a relative amplitude mismatch between the two 3-port mixers. The mixer equation including these factors can be modeled as:

$$V_{RF}(t) = \mathrm{Re}\left\{z(t)\left[\cos(\Omega t) + ir_{up}\sin\left(\Omega t + \phi_\delta\right)\right] + \epsilon e^{i\Omega t}\right\} \tag{1.24}$$

where $z(t) = I(t) + iQ(t)$, $r$ is the amplitude mismatch, $\phi_\delta$ is the phase imbalance and $\epsilon$ is the magnitude of LO leakage. It is clear that adding a DC offset to $z(t)$ can eliminate LO leakage, adjusting amplitudes of $I, Q$ can lead to $r \to 1$ and appropriately adjusting their relative phase leads to $\phi_\delta \to 0$.

### 1.7.4 Modulation Schemes

In practical situations, even a small leakage signal can drive the qubit. Therefore we need to ensure that only the signal we desire reaches the qubit. We employ different schemes in different setups:

**IQ Mixers:** We employ a technique called *Single Side Band* (SSB) modulation in IQ mixers, where the two quadratures $I(t), Q(t)$ are chosen to be $90^o$ out of phase. Mathematically $V_{RF}$ in this case becomes,

$$\begin{aligned} V_{RF} &= \cos(\omega_{IF}t) \times \cos(\omega_{LO}t) + \sin(\omega_{IF}t) \times \sin(\omega_{LO}t) \\ &= \cos((\omega_{LO} - \omega_{IF})t) \end{aligned} \tag{1.25}$$

i.e., one of the sidebands gets canceled out due to destructive interference. In the equation above, the $(f_{LO} + f_{IF})$ frequency is canceled. If $Q(t)$'s phase is shifted by 180 degrees, the $(f_{LO} + f_{IF})$ frequency will survive. This process is called 'up-conversion'. However, if the RF port is used as an input, and IF port is used as an output, the process is called 'down-conversion' and is used for qubit readout as shown in figure (2.3). As discussed in the previous section, the I(t) and Q(t) signals can be adjusted to minimize LO leakage and the unwanted sideband. However, this requires extensive calibrations, which can drift with time due to temperature fluctuations and other noise channels. These calibrations therefore have to be repeated periodically for maintaining the accuracy of the control pulses.

**Three-port Mixers:** When dealing with three-port mixers, the SSB modulation is not possible. Therefore, we require filtering to reduce the unwanted sideband and LO leakage. Since IF frequencies are usually small (a few 100 MHz), the filtering requirements tend to be challenging. Moreover, the filtering requirements will vary for different output frequencies for controlling qubits and readout cavities at different frequencies. This makes a given setup less flexible in terms of operation over a wide range of frequencies.

Both the schemes have some disadvantages. The IQ mixer setup mentioned above requires two IF channels and has to be periodically calibrated to maintain accuracy. On the other hand, the three-port mixer setup, while needing only one IF channel, has stringent filtering requirements. An arbitrary waveform generator is typically used to generate the IF signals and is a more expensive resource than filters. As one scales up to a large number of qubits, it would be immensely beneficial to reduce the IF channel count. Further, not requiring periodic calibrations helps maximize the usable time in a quantum computer. Keeping these arguments in mind, we now discuss a method to use a three-port mixer in a practical setup for creating qubit and readout control signals.

### 1.7.5 Two-stage frequency up-conversion

Let the IF frequency have at frequency $\omega_{IF}$, phase $\phi$ and amplitude $A(t)$. Without loss of generality we can assume $\omega_{IF} < \omega_{LO1}$. Therefore, following equation (1.24) after the first mixer, we have:

$$\begin{aligned} S_1(t) =& A(t)\sin(\omega_{LO1}t + \theta_o)\sin(\omega_{IF}t + \phi) + \alpha(t,T)\sin(\omega_{LO1}t + \theta_o) \\ =& \frac{A(t)}{2}\left[\cos((\omega_{LO1} - \omega_{IF})t + \theta_o - \phi) + \cos((\omega_{LO1} + \omega_{IF})t + \theta_o + \phi)\right] \\ & + \alpha(t,T)\sin(\omega_{LO1}t + \theta_o) \end{aligned}$$

The signal passes through a bandpass filter designed to reject the lower sideband $(\omega_{LO1} - \omega_{IF})$ as well as the LO frequency $(LO_1)$. Therefore, only the upper side-

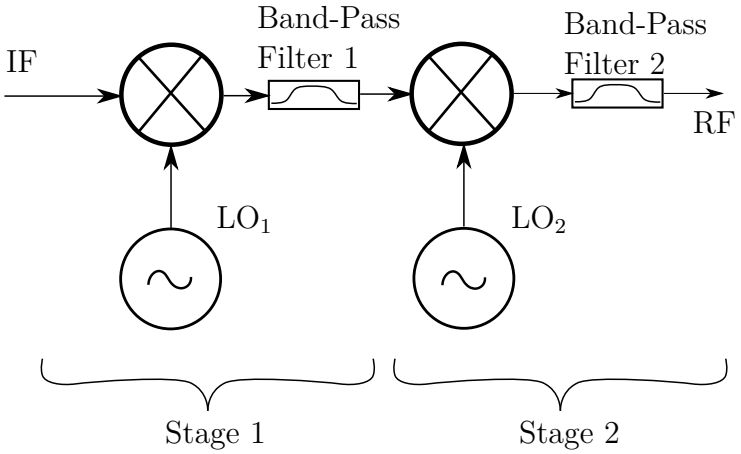


Figure 1.6: The basic double frequency up-conversion scheme.

band survives to mix with the second LO frequency ($LO_2$). Taking $\phi_1 = \theta_0 + \phi$, we have

$$\begin{aligned} S_2(t) =& \frac{A(t)}{2}\sin((\omega_{LO1}+\omega_{IF})t+\phi_1)\sin(\omega_{LO2}t+\phi_2) + \beta(t,T)\sin(\omega_{LO2}t+\phi_2) \\ =& \frac{A(t)}{4}\left[\cos((\omega_{LO1}+\omega_{IF}+\omega_{LO2})t+\phi_1+\phi_2) + \cos((\omega_{LO1}+\omega_{IF}-\omega_{LO2})t+\phi_1-\phi_2)\right] \\ & + \beta(t,T)\sin(\omega_{LO2}t+\phi_2) \end{aligned}$$

This signal again passes through a bandpass filter designed to reject $\omega_{LO2}$ and the upper sideband $(\omega_{LO1} + \omega_{IF} + \omega_{LO2})$. Hence we have our final signal as:

$$S_{RF}(t) = \frac{A(t)}{4} \times \cos((\omega_{LO1} + \omega_{IF} - \omega_{LO2})t + \theta_0 + \phi + \phi_2)$$

where we have a constant non-varying phase difference and no LO leakage.

The above setup, also known as super-heterodyne, thus gets rid of the need to calibrate DC and phase offsets with time and the two stage upconversion process simplifies the filtering requirements. Note that the filtering challenge comes from the fact that the IF signals are typically low frequency ($\sim 100 - 200$ MHz) signals which results in small frequency separation between the desired and unwanted signals. In principle, this can be solved by using a high frequency ($\sim 2-3$ GHz) IF signals but high speed DACs are typically more expensive. In this superheterodyne setup, the first stage of up-conversion can be thought of as an alternative way to create an effective high frequency IF signal for the second stage. The filtering requirement for the first stage is not complicated because the frequencies involved here are fixed. The output of the first stage is always at a fixed center frequency with a modulation specified by the low frequency IF signal. Once the

output frequency of the first stage $\mathrm{RF}_{out} = (\omega_{LO1} + \omega_{IF})$) is high enough, it renders a huge separation of the bands produced in the second up-conversion. This gap allows easy filtering of the required band. Further, since super-heterodyne allows using a wider band-pass filter, we can generate output over a broader frequency range, thus eliminating the need to construct new filtering setups. Recently, new commercial RF instruments have started implementing this scheme, one example being from Zurich Instruments [2].

In this thesis, we will attempt to implement a slightly modified version of this technique for qubit control and measure the stability of single qubit gates. As described in the next section, we implement the first stage up-conversion using a digital mixer inside a *Xilinx RF System on Chip (RFSoC)* to create an IF signal at 2.5 GHz.

### 1.7.6 RF System on Chip

Recently, FPGA based modules for direct generation of microwave signals have been engineered for 5G technology. One such module is the RFSoC FPGA board by Xilinx[3], which offers up to 9.8GSPS sampling rates. Therefore, one can theoretically produce up to 4.9GHz reliably. Further, one can also use multi-Nyquist techniques to create output signals higher than the sampling rate to digitally generate microwave frequency signals in the range relevant for superconducting qubits ($4 - 8$ GHz) [15].

In this work, we are exploiting the digital mixing capabilities available on the RFSoC to implement the first stage of the up-conversion process. This was done partially for convenience and also due to lack of availability of appropriate mixers in the lab. In digital mixing, a lower frequency IF signal is digitally multiplied with a higher frequency LO signal from a numerically-controlled oscillator near the DAC. The final multiplied/upconverted data is then streamed to the DAC. These mixers rely on numerical multiplication and are completely ideal, and therefore do not suffer from standard analog mixer non-idealities.

[2] https://www.zhinst.com/sites/default/files/documents/2022-07/zi_shfsg_leaflet.pdf
[3] https://www.xilinx.com/products/boards-and-kits/zcu216.html

# Chapter 2

# Experimental Methods

In this chapter, we discuss the experimental setup as well as methods used to fabricate, cool down, detect, control and measure quantum superconducting circuits. We also present the implementation of the super-heterodyne setup.

## 2.1 Fabrication

For our experiments, we used a transmon in a 3D cavity. We begin by discussing the fabrication of transmon. As evident in the section (1.3), to fabricate a functional qubit, we require a capacitor and a Josephson junction (JJ) with particularly precise characteristics. Fabrication of the JJ begins by spin coating a stack of two organic resists on the silicon wafer. One relatively thick ( $400 - 450nm$) soft resist (EL9) is placed beneath a harder (AR) and thin ($200nm$) resist. This is done in order to enable a suspended bridge for fabrication of the JJ, called the Dolan bridge technique [8]. A 28keV e-beam is then radiated onto the resist, de-linking its polymer chains. This step patterns the shapes of the transmon onto the resist. The exposed resist is chemically removed, leaving a stencil on the chip. This stage is called the development of the resist and is usually followed by a plasma cleaning procedure to remove the exposed resist completely. At this point, we have a silicon substrate with a stencil of a transmon and a bridge, as shown in the schematic. To create an insulating barrier, we perform directional electron beam evaporation at two angles separated by a controlled oxidation step. Finally, a second controlled oxidation follows to help the junction age reliably and in a controlled fashion. The device is then submerged in acetone and followed by sonication to remove the stencil mask from the substrate, called a lift-off, and we are left with a transmon [9] [4].

The design characteristics of the transmon are mainly controlled by the junction area and the thickness of the oxide layer, which heavily depends on the angle of

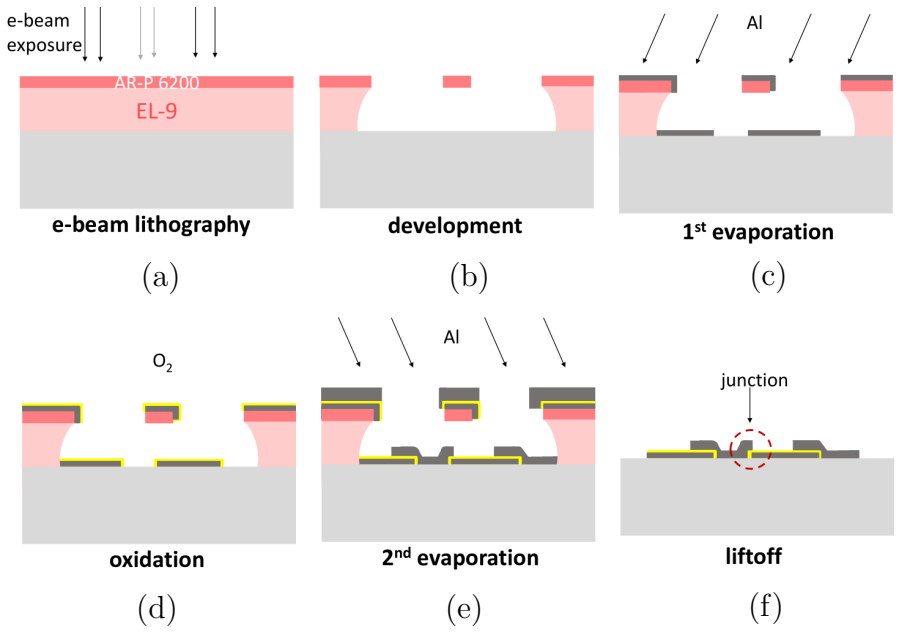


Figure 2.1: The fabrication process is depicted step-wise with the Dolan bridge technique[8]. (a) The hard and soft resists are spin coated on top of the silicon substrate (grey). Then the resist is patterned using an e-beam. (b) The resist is chemically removed, and later plasma (oxygen) etched. The Dolan bridge can be seen as the suspended block. (c) Aluminum is evaporated onto the substrate at an angle. (d) A controlled oxidation step leads to a oxide layer ($\sim 1-2$nm). (e) Post-oxidation another evaporation is done at a different angle to form the junction. (f) The remaining substrate is lifted-off by acetone and sonication.

evaporation and the controlled oxidation step respectively. We use aluminum for our transmons, which has a $T_c = 1.1K$ and a gap of $\Delta \simeq 200\mu V \rightarrow 100GHz$ [2]. The RF frequencies we design our qubit in, are an order lower(1.3), as well as the temperatures at which we will test our qubit, have an infinitesimally small amount of radiation in this regime (refer section 2.2).

## 2.2 Cryogenic Setup

In order to detect and probe the qubit, the temperature must be set such that $\hbar\omega_q \gg k_B T$, i.e., the energy needed to excite the qubit must be well below the thermal noise. For the usual design of 5GHz transition frequency, the temperature is about 240mK. Therefore, we need cryogenics to do our experiments. The experiments presented in this thesis have been done in an *Oxford Instruments Proteox* dilution refrigerator. The fridge wiring, as shown in schematic (2.2), has

stages of thermalization, each at a different temperature. There is a 300K plate at room temperature, a 60K plate (PT1), a 4K plate (PT2), a 700mK plate (Still), a 150mK plate (Cold plate), and finally, a base plate at 10mK. Each of these plates is shielded by annular radiation shields. The sample is placed inside yet another radiation shield which can be superconducting based on the application.

As is evident from the schematic (2.2), we require multiple stages of RF electronics inside the fridge to set up control and readout. We ensure no noise from any component at high temperature reaches the sample. As it enters the fridge, the input (qubit/readout) line has a corresponding 300K Johnson–Nyquist noise. This noise needs to be attenuated heavily ($\sim 60dB$). Therefore, attenuators are placed at different stages in the refrigerator such that they only add noise of their temperature further in the chain. The last attenuator is kept at the base temperature. There is a custom made *Eccosorb* filter that is designed to offer 7dB (HLF) and 3dB (LLF) of attenuation at the cavity frequency and absorbs all high-frequency noise ($\sim$ 100s of GHz) to protect the superconducting nature of the qubit.

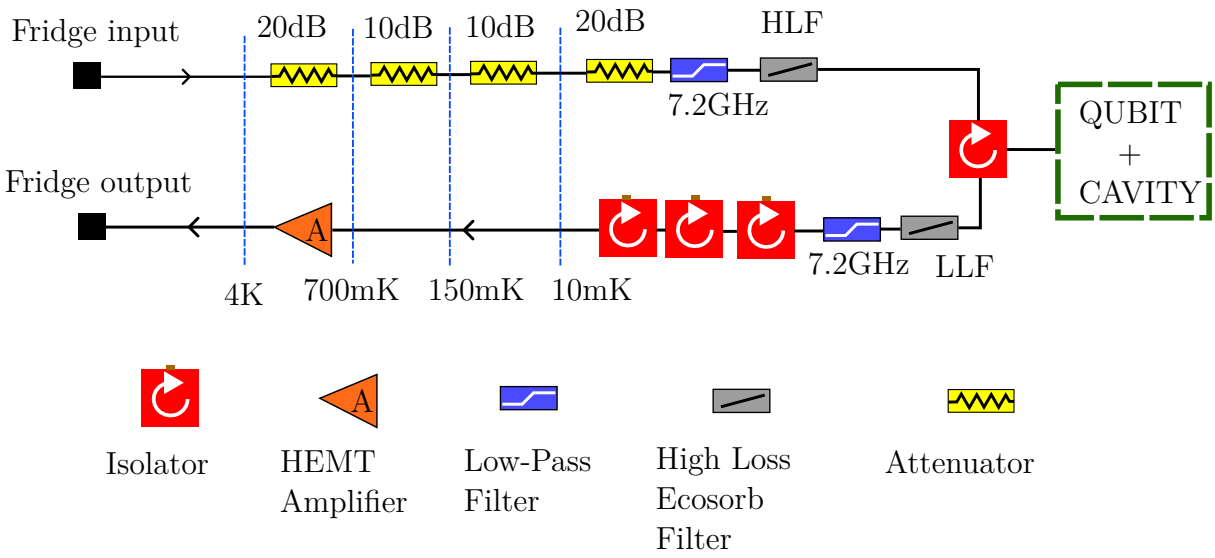


Figure 2.2: (color) The wiring diagram of the cryogenic setup employed in the thesis. The circuit is built inside the dilution fridge.

A signal coming from the input line finally goes through a circulator and reaches the qubit-cavity system. The signal interacts with the system and reflects. The reflection from the qubit-cavity system gets transmitted to the output/readout line. The output line brings the signal from the qubit to the room temperature setup. It cannot have any attenuators as it would attenuate the signal from the qubit. We have a high electron mobility transistor (HEMT) amplifier at the 4K stage on the output line, which provides sufficient amplification so that the room

temperature noise does not significantly affect the SNR. In some cases we also employ nearly-quantum limited amplifiers, called Josephson parametric bifurcation amplifiers [10] to amplify the signal at the base temperature. To prevent any noise from the amplifier from reaching the qubit, we employ a series of isolators [1] in the readout line.

## 2.3 Room Temperature Setup

Besides the cryogenic setup, microwave/RF electronics at room temperature are used to generate pulses for control and readout [2] of the qubit. We employ two different setups, one consisting of a standard setup and the other consisting of the superheterodyne setup. Both are depicted in the schematic (2.3).

### 2.3.1 Standard Setup

In the standard setup, we follow the Single Side Band modulation scheme, discussed in section (1.7.4). The control pulses are generated at 150MHz with appropriate I and Q envelopes ($1V$ peak-to-peak) directly from the OPX. These are fed to a *Marki IQ-0307* mixer and up-converted to the qubit frequency with SSB modulation. A low noise *Rhode & Schwartz RF source* generates the LO tone for the mixer and is set to 13dBm output power. Since the cavity is detuned from the qubit, we require driving the qubit with much more power; therefore, we amplify our control signals. The tone for readout is generated similarly, sans the amplification. These two tones are combined[3] and sent to the qubit input in the fridge. The reflected signal from the fridge returns from the 'Fridge-out' line and is amplified & fed into a demodulation mixer in the 'Digitizer' line. The LO tone for the demodulation mixer is obtained from the same RF source as the readout up-conversion mixer to track the phase difference in the reflected signal. The de-modulated I and Q signals are sent to a low-noise pre-amplifier before finally digitizing them.

[1] An isolator is just a circulator with one port terminated at 50Ω. Since all the other lines are matched to 50 Ohms, there are no reflections and an isolator acts like a non-reflective diode.

[2] "Readout" is used colloquially to refer to measurement and the input/output line corresponding to the measurement of the qubit.

[3] The combiner/splitter used here is a passive three-port RF component that divides power received from the input port equally between two output ports. Since the component is passive, it can be used to 'combine' signals as well. [7]

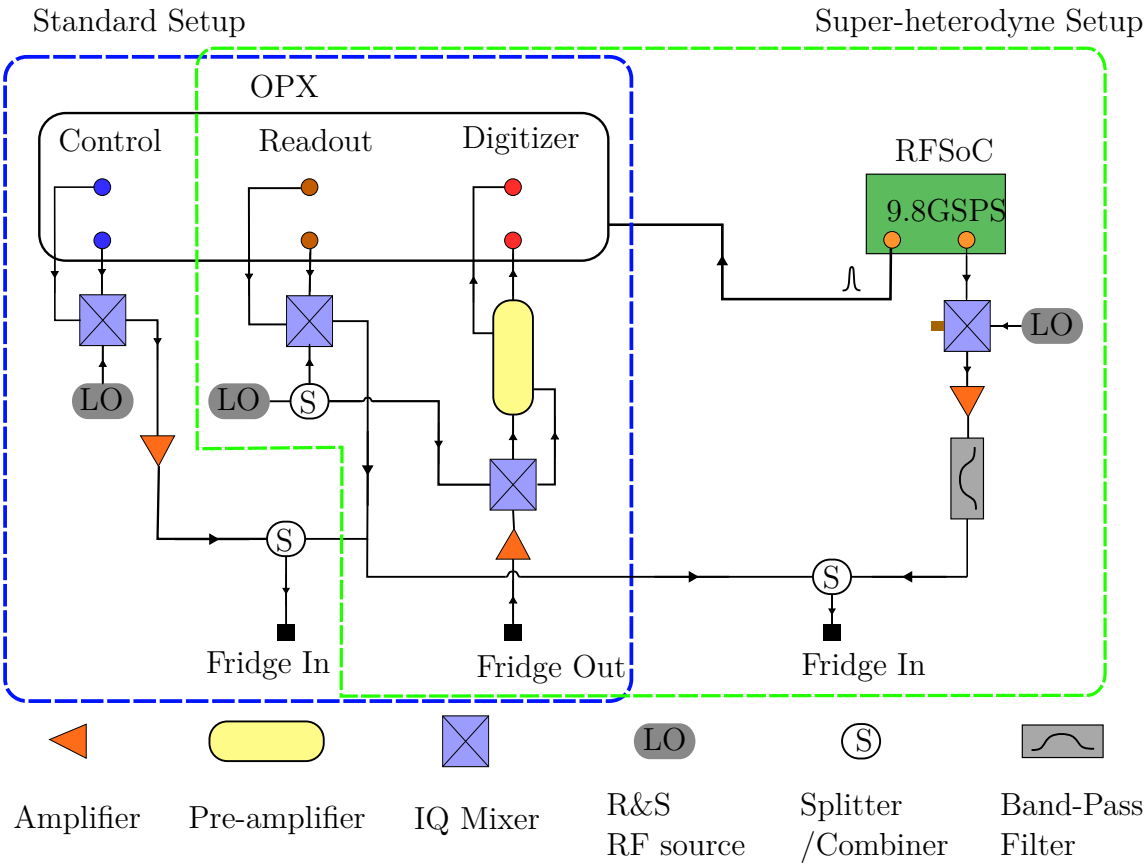


Figure 2.3: (color) A schematic of the room temperature setup. The standard setup is outlined by a blue boundary and the superheterodyne setup has been outlined by a green boundary. **Note that only one of the two setups is used at a time**. The Xilinx RFSoC has DACs capable of sampling at 9.8 GSPS. The QM's OPX system consists of DACs and ADCs sampling at 1 GSPS. A trigger is sent from the RFSoC to the OPX to begin readout when the qubit control sequence ends.

### 2.3.2 Superheterodyne Setup

The superheterodyne setup discussed in section (1.7.5) proposed two mixer stages. It is important to realize that the first mixer stage is used to create a high IF frequency for the second stage such that the second up-conversion renders a big gap between the bands and is therefore easier to filter out. As mentioned earlier, we use the RFSoC board to implement the first stage of up-conversion using digital mixing. The second stage remains unmodified as depicted in figure (2.3).

The superheterodyne setup therefore is left with two main components - the second stage mixer and the second stage filter. Since we require a broader range of operation, we choose the *Marki MMIQ-0520HSM* mixer which supports IF of up to 6GHz and RF/LO between 5GHz to 20GHz. We use an IQ mixer, however,

we terminate one IF port of the mixer with an impedance matched 50Ohm terminator to essentially use the IQ mixer as a three port mixer (refer to figure 1.5). The filtering requirements need a custom fabrication of a filter with desired characteristics. In this thesis, we fabricate a coupled-line Band-Pass filter using the *iFilter Wizard* in Cadence AWR Microsoft Office software, AutoCAD and LPKF PCB prototyping machine. The design choices as well as fabrication are discussed in Chapter 3.

Therefore, as depicted in the figure (2.3), the setup in this case is simply the IF signal being generated from the RFSoC, up-converted using an IQ mixer with one port terminated at 50 Ohms, finally amplified and put through a band-pass filter to reject LO leakages and the upper side band. This line is then combined with the readout line as in the standard setup and transmitted to the fridge input.

## 2.4 Cavity Characterization

Qubits are placed inside resonator cavities. The cavities are high Q cavities with precisely calibrated coupling to the outside environment. As discussed in section (1.4), we limit ourselves to the first mode of the cavity, i.e. the $TE_{101}$ mode. We choose the dimensions to be $\sim$ 3cm $\times$ 0.8cm $\times$ 6mm, such that the cavity resonant frequency is about 7GHz. We design 3D models of the cavity in a CAD software and employ numerical simulations to estimate the resonant frequency in softwares such as Ansys HFSS. Since finite element methods can account for geometry imperfections, input/output connectors and the silicon chip, it allows us to be more realistic while designing the cavity. The cavity is then precision machined into a bulk of Aluminum/Copper depending on requirements.

The cavity is characterized by its line-width and its internal & external quality factors. The cavity line-width $\kappa$ can be determined by measuring the reflection $S_{11}$ from the cavity. The real part of the power received can be fit to a Lorentzian:

$$\text{Real}|S_{11}| = \frac{A}{(x-\omega_c)^2 + \kappa^2/4} \tag{2.1}$$

The phase shift obtained across resonance is intimately related to the line-width. The phase of the reflected signal shifts by $\pi$ across the resonance of the cavity.

$$\theta = \arctan \frac{2}{\kappa}(\omega_c - \omega) \tag{2.2}$$

Near the resonant frequency $\theta$ is inversely proportional to $\kappa$. Hence the amount of phase shift encountered when qubit switches between $|g\rangle$ and $|e\rangle$, is dependent on $\kappa$.

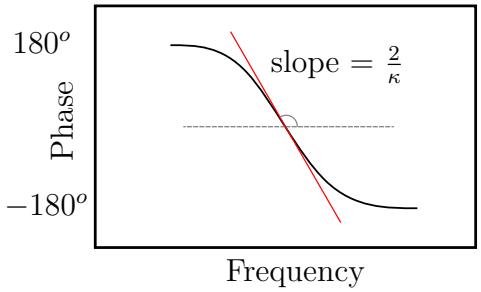


The external quality factor is adjusted by the length of the pin protruding inside the cavity. It represents the coupling to the environment, therefore the ability to drive the qubit as well as the loss to the environment are controlled by this value. The internal cavity quality factor is a measure of the losses due to the cavity and the qubit chip. The total quality factor is just the parallel combination of these:

$$\frac{1}{Q_{tot}} = \frac{1}{Q_{int}} + \frac{1}{Q_{ext}} = \frac{\kappa}{\omega_c} \tag{2.3}$$

The external quality factor is designed to dominate the internal i.e., we expect the cavity to be over-coupled to the input port.

## 2.5 Frequency Domain Spectroscopy

After cooling down our qubit and cavity system, we start by probing the cavity to check if our qubit is functional. We start by attaching a Vector Network Analyzer (VNA) to the control and readout and measure the amplitude $\log|S_{11}|$ and the phase $Arg(S_{11})$ of the reflection ($S_{21}$ measurement on the VNA). We choose the power to be low enough such that the qubit does not get excited, since they are far detuned (refer section 1.5). Therefore, we measure the resonant frequency of the cavity when qubit is in the ground state. Then, we increase the power of the VNA, such that the electrical currents induced in the qubit are higher than the critical current of the Josephson junction. In this regime, the qubit is non-existent and we get the true cavity response. This is called *'punch-out'*. If these frequencies are different, we can deduce that the qubit is functional. This also implies that we can detect the qubit's state (which changes the cavity frequency) depending on the phase shift we experience in the reflected signal.

After we ascertain that the qubit is working, we move on to find the qubit frequency. At this point, we are certain we will see a phase shift in the reflected signal depending on qubit state. We move to the setup shown in schematic (2.3) and sweep frequencies near the expected qubit frequency and follow it with an immediate cavity response (readout) measurement. In this case we measure the $\log|S_{11}|$. We send in high power and immediately see two peaks (refer fig. 2.5

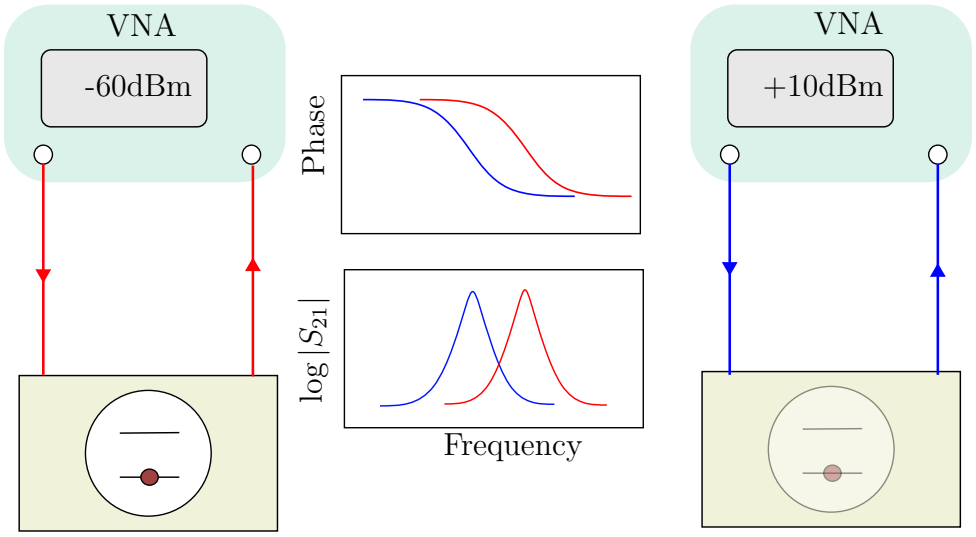


Figure 2.4: (colour) The setup used for punch-out spectroscopy. The resonant frequency of the qubit + cavity system is higher when the qubit is at a lower frequency than the cavity. A corresponding phase response is also shown.

and fig. 3.2). The sharper peak corresponds to the two photon $0 \rightarrow 2$ transition (called 02/2 peak) and the broader peak corresponds to the $\omega_{01}$ transition. We decrease the power and see the 02/2 peak disappear as number of photons in the cavity decrease. The $\omega_{01}$ peak becomes sharper and is typically ascertained upto a MHz.

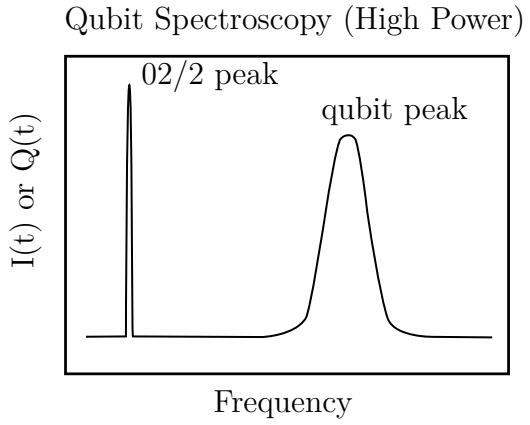


Figure 2.5

## 2.6 Time Domain Measurements

Since we now know the qubit frequency and the cavity frequency, we can now begin probing qubit dynamics. We employ the control and readout setup shown in figure (2.3) and start time-domain experiments in the order shown:

### 2.6.1 Rabi measurement

The first experiment in time domain measurements is to see Rabi Oscillations. This experiment is done by sending a control pulse/qubit signal for a time '$t$' and immediately following it with a measurement pulse/readout. Looking back at

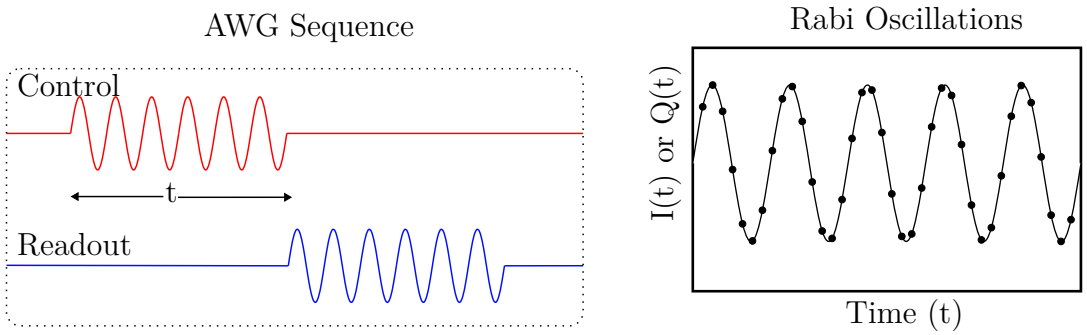


Figure 2.6: The control sequence of the Rabi measurement is shown. Time '$t$' of the pulse varies and excites the qubit to different points on the Bloch sphere, which shows up as sine oscillations (right), corresponding to a motion in a circle on measurements.

equation (1.21) we can see that the probability and the separation in $I(t)$ or $Q(t)$[4] between the $|0\rangle$ and $|1\rangle$ state depends inversely on the detuning $\delta_d$. Similarly, being far detuned also leads to faster oscillations as explained in the figure (1.2). Usually we are not detuned by more than a MHz (refer 2.5) and can see the oscillations with enough amplitude.

### 2.6.2 Power Rabi measurement

For our next experiment, we try to calibrate $\pi$ and $\pi/2$ pulses to be able to prepare the qubit into a variety of states. We begin by calibrating $\pi$ and $\pi/2$ pulses. From the previous Rabi experiment, we get a rough idea of realizable lengths of our $\pi$ pulse. We fix our pi-pulse length to an acceptable length (say 70 ns) and then sweep the power/amplitude of our control pulses (figure 2.7).

[4]The required phase information can be extracted out of any one channel ($I(t)$ or $Q(t)$). Therefore, one can digitally rotate these vectors such that amplitude is maximized in either of the channels.

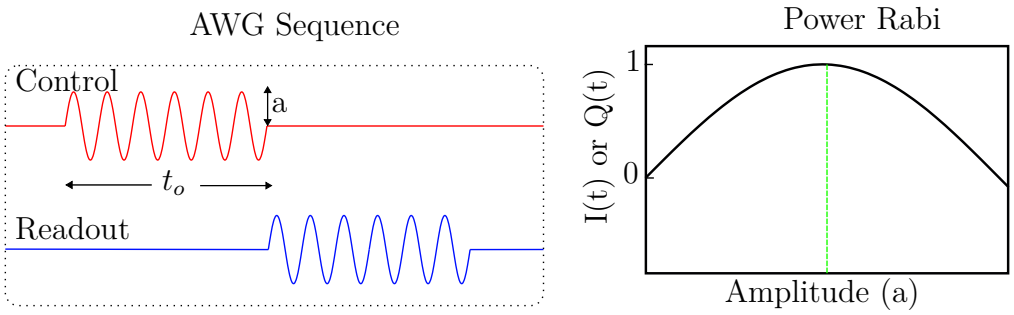


Figure 2.7: The scheme for Power Rabi consists of sweeping in amplitude for a fixed $t_0$ pulse length. The first maxima we observe in this graph will represent the first complete $\pi$ rotation.

We can further focus on the exact pulse by adding more $\pi$ or $\pi/2$ pulses in our control sequences. With $(2N+1)$ number of $\pi$ pulses in the control sequence, we can effectively force the qubit to traverse multiple rotations. Any $\epsilon$ error per rotation gets magnified after repeated rotations, hence, only for very accurate amplitudes the qubit evolves to the state $|e\rangle$. In the experiment, we see an increased number of peaks as we increase N, and therefore, each peak becomes sharper and precise. Similarly, in the case of calibrating $\pi/2$ pulses, we send $(4N+2)$ number of pulses - so that the qubit reaches $|e\rangle$ - to the fridge and repeat the Rower Rabi experiment.
We can simply fit the curve obtained to a sine function and extract the amplitude for which the sine function is maximum. This calibration will then be refined further in section (2.7).

### 2.6.3 Ramsey measurement ($T_2^*$)

Since we now know our qubit is alive and our pulses are characterized, we can observe the dynamics of dephasing. For this we employ the Ramsey measurement where we set up our control sequence to have two $\pi/2$ pulses separated by a variable time interval. When the time interval exactly corresponds to the dephased angle of $\pi$, we get an excited state[5].
The Ramsey curve obtained can be defined as the function:

$$Q(t) = A + B\sin(2\pi\Delta_d t + \phi)\exp\left\{\frac{t}{T_2^*}\right\} \tag{2.4}$$

On a finite detuning, we obtain a sinusoidal curve. By fitting this curve we can refine our qubit frequency upto a few KHz (compared to almost a MHz in qubit

[5]Given that the next pulse is also $180^0$ phase shifted, otherwise, the excited state would come at $2\pi$ dephased angle.

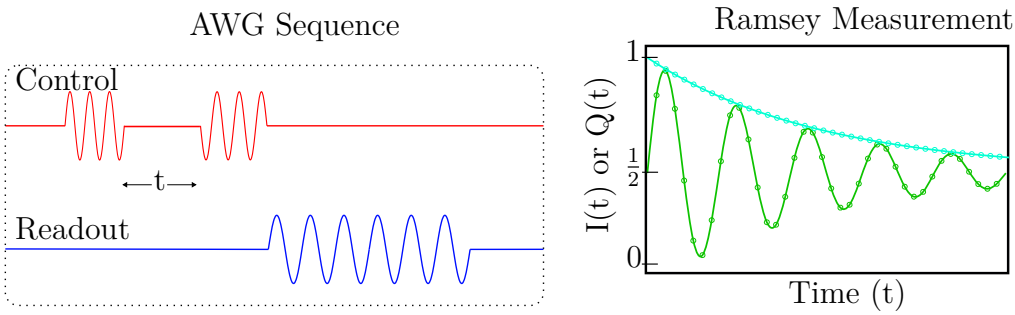


Figure 2.8: The control sequence of a Ramsey experiment is two $\pi/2$ pulses separated by a time '$t$'. We obtain decaying sinusoid if drive is detuned from the qubit frequency. If the drive is perfectly aligned, we get the exponential decaying to the mixed state.

spectroscopy in section (2.5)).

### 2.6.4 $T_1$ measurement

After fixing our drive frequency to the exactly the qubit frequency, we can now drive the qubit resonantly and measure the decay/bit flips of the qubit. This characterizes the the lifetime of the qubit. In the control sequence, we put the qubit in an excited state with a $\pi$ pulse and wait for a variable time '$t$' before measuring. The qubit relaxes to the ground state spontaneously with time. The data obtained can be fit to a decaying exponential:

$$Q(t) = A + B \exp\left\{\frac{-t}{T_1}\right\} \tag{2.5}$$

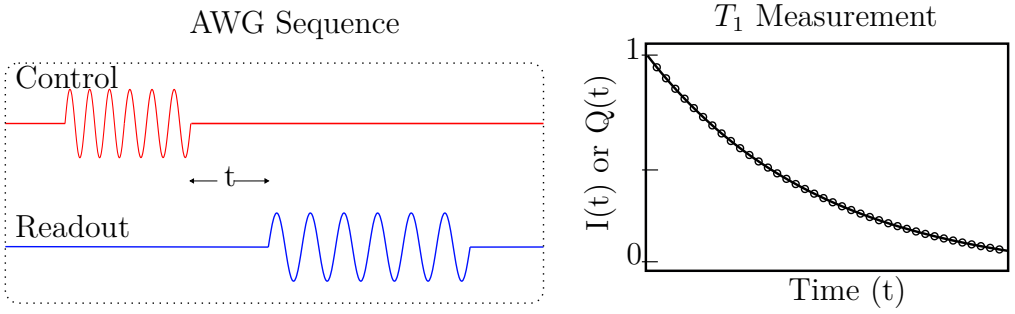


Figure 2.9: Control sequence for measuring $T_1$ decay times.

### 2.6.5 Hahn Echo measurement ($T_{2E}$)

Hahn Echo (or *spin echo*) measurement is used to characterize the phase decay time $T_{2E}$. The Echo measurement is robust against detuning and qubit state decay

$T_1$. In the control sequence, we put the qubit to a superposition state with a $\pi/2$ pulse, wait for time '$t/2$', flip the qubit state by a $\pi$ pulse, again wait for time '$t/2$' and perform readout. The $\pi$ pulse leads to the cancellation of the slow noise of the qubit. The slow noise arises out of Larmor precession if the qubit drive is slightly detuned from the actual qubit frequency.

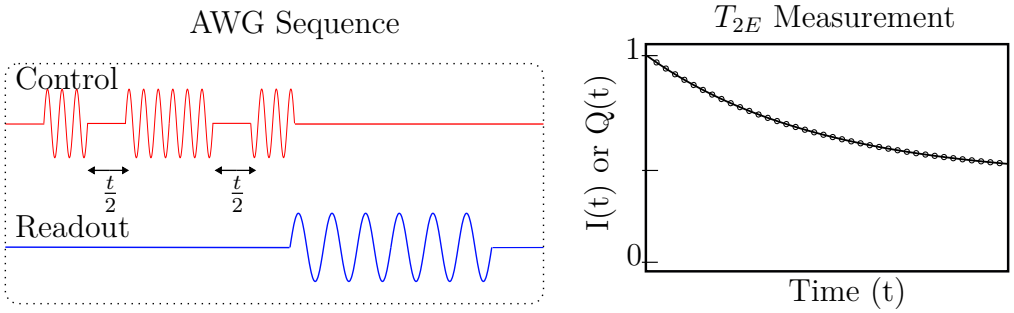


Figure 2.10: Control sequence for measuring $T_{2E}$ decay times.

The measurements are fitted to:

$$Q(t) = A + B \exp\left\{\frac{t}{T_{2E}}\right\} \tag{2.6}$$

Since echo measurement gets rid of slow noise affecting the qubit-cavity system, it is a more relevant measure of a qubit's coherence times.

## 2.7 Calibration & Stability: Bang-Bang Measurement

With the qubit fully characterized and pulses calibrated, we can conduct a more detailed study of the qubit and its calibrations. A standard $\pi$ pulse has a duration of tens of nanoseconds. The timing resolution of DACs in AWGs is typically much poorer than the amplitude resolution. Therefore, we fix the pulses in time and perform more precise calibrations in terms of pulse amplitude. One of the techniques used for this purpose is the Bang-Bang measurement.

The Bang-Bang scheme, which is derived from control theory, involves switching between two states of a system. In our experiments, we apply repeated identical pulses on the qubit, effectively switching it between different states, until the error begins to amplify. The pulse amplitude is then iteratively adjusted and tested with a longer sequence of pulses until a desired accuracy is achieved.

As seen in Equation (1.20), the rate of change of probabilities is highest at $\theta = 0$, indicating that the qubit is most sensitive to mis-calibrations when measured

in a perfect superposition state, or when the Bloch vector is located at the equator. Therefore, we always prepare the qubit in a $|\pm\rangle$ [6] state prior to the experiment, as well as adjust the control sequence such that the final expected state is $|\pm\rangle$.

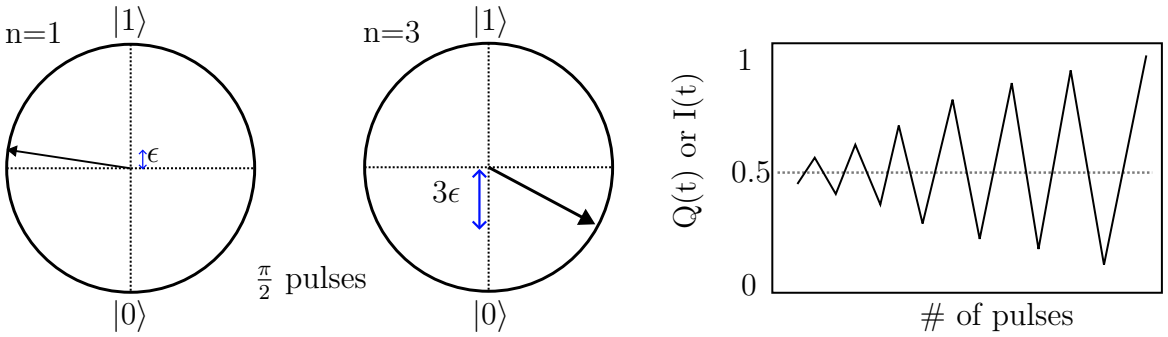


Figure 2.11: The errors as shown grow with repeated pulse application. The error in one pulse ($X_{\pi/2}$) is $\epsilon$ [11], with $n$ pulses it grows to $n\epsilon$. This magnified error can then be calibrated for with fine adjustments in amplitude. The corresponding error in angle is $\epsilon^2/6$ radians for an $\epsilon$ error in $\sigma_z$ [12]. An odd number $\pi/2$ pulses are applied such that the bloch vector ends up in the $|\pm\rangle$ state.

The data can simply be fit to a function where the probability of measuring zero is [9]

$$P(|0\rangle) = a + \left[\frac{1}{2}(-1)^n \cos(\pi/2 + 2n\epsilon)\right] \tag{2.7}$$

where $a \to 0.5$ and $\epsilon$ is the error.

Since the method is based on error amplification, a small erroneous deviation is also detectable. Therefore, a series of repeated bang-bang measurements over an extended period of time can serve as a means of assessing fluctuations in the amplitude and general stability. In chapter 3, we will use the results of Bang-Bang measurements to comment on the stability of our setups.

[6] $|\pm\rangle := (|0\rangle \pm |1\rangle)/\sqrt{2}$

# Chapter 3

# Experiments and Analysis

Utilizing the experimental setup and understanding of the experiments described in previous chapters, in this chapter, we present the results of measurements performed on a transmon qubit placed in an aluminum cavity.

## 3.1 Frequency Domain Measurements

As outlined in Section (2.5), we initiated our analysis by measuring the cavity response. The real part of the reflection and the phase response of the cavity are depicted in Figure (3.1).

To extract further information, the real part of $S_{11}$ was fit to a Lorentzian function (as detailed in Equation 2.1). The resulting data extracted from this analysis is:

- At -35dBm (low) power, the resonant frequency is $7.340345 \pm 0.000002$ GHz.
- At 3dBm (high) power, the resonant frequency is $7.338586 \pm 0.000002$ GHz.
- The external bandwidth of the cavity, $\kappa_{ext} = 1.166 \pm 0.004$MHz.
- The internal bandwidth of the cavity, $\kappa_{int} = 0.273 \pm 0.004$MHz.

The cavity is operating in the over-coupled regime as intended. As demonstrated in Figure (3.1), the cavity exhibits a "punched-out" response at an input power of 3dBm. Additionally, a shift in the resonant frequency of the cavity, on the order of $\sim 2$MHz ($= g^2/\Delta$), is discernible from the change in phase. These observations allow us to infer that the qubit is functional, and we can proceed to conduct qubit spectroscopy to determine the qubit's resonance frequency.

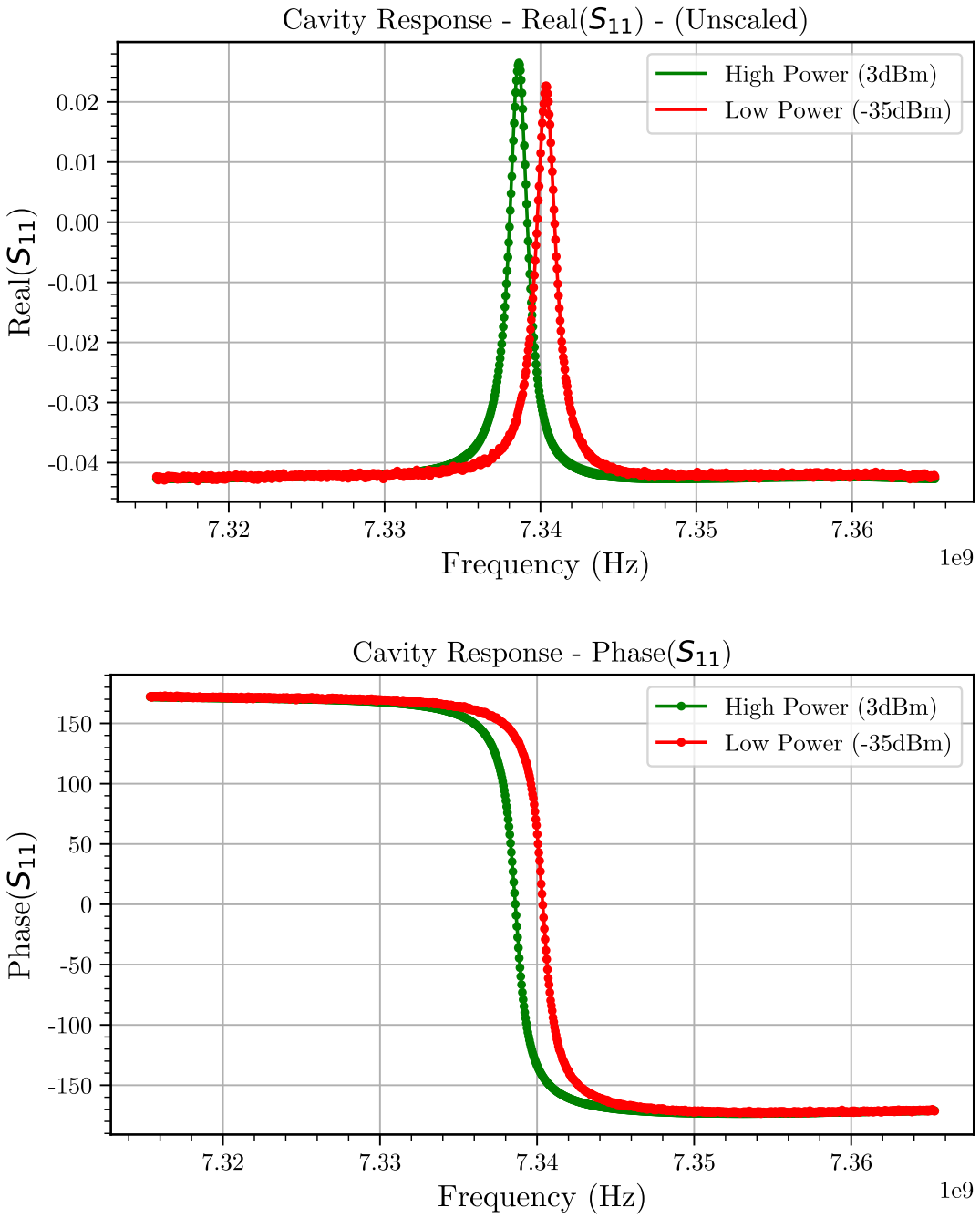


Figure 3.1: (colour) Cavity response at low temperature. The reflection is measured at different frequencies.

In the following experiments, we have transitioned to the room temperature

setup as outlined in Figure (2.3). All calibrations required are done and not mentioned in this thesis. Standard qubit spectroscopy as mentioned in section (2.5) is employed. The initial scans were conducted at high power, with peaks ranging from 4.5 to 5.5 GHz, as the qubit's designed resonance frequency lies within this range.

Upon examination at high power, we observed two distinct peaks, as anticipated and depicted in Figure (3.2). The sharp peak on the left corresponds to the $\omega_{02}$ two-photon transition process, commonly referred to as the '02/2' peak. The second, broader peak corresponds to the $\omega_{01}$ transition, which will be utilized for all subsequent experiments. To further investigate the qubit peak and reduce peak broadening, we proceeded to probe the peak at lower power, thus allowing us to ascertain the peak to within 500 KHz (refer to Figure 3.3).
The following data is extracted from the graphs:

- $\omega_{02}/2 \rightarrow 5.0493 \pm 0.0005$GHz
- $\omega_{01} \rightarrow 5.1961 \pm 0.0005$GHz
- Anharmonicity, $\alpha = 2 \times (\omega_{02}/2 - \omega_{01}) = -293 \pm 1$MHz.

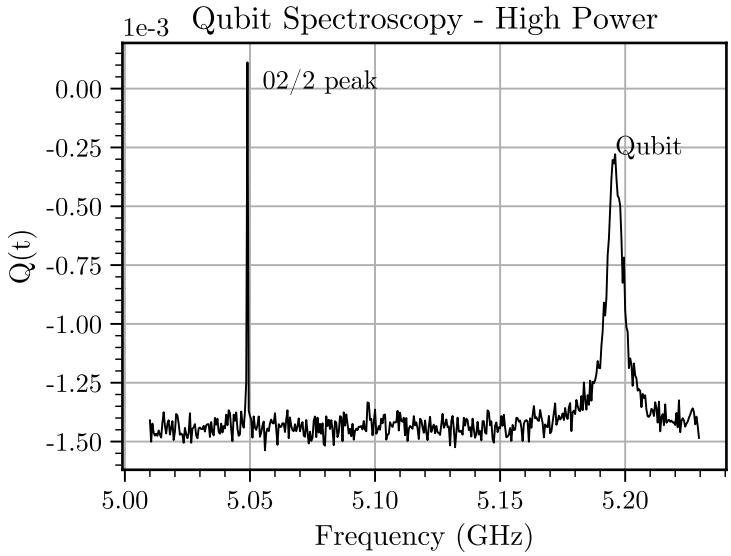


Figure 3.2: The frequency response as seen at high power. The sharper peak is the two photon $0 \rightarrow 2$ transition. The $0 \rightarrow 1$ (qubit) peak is power broadened. The qubit peak is the furthest peak found in the entire spectrum.

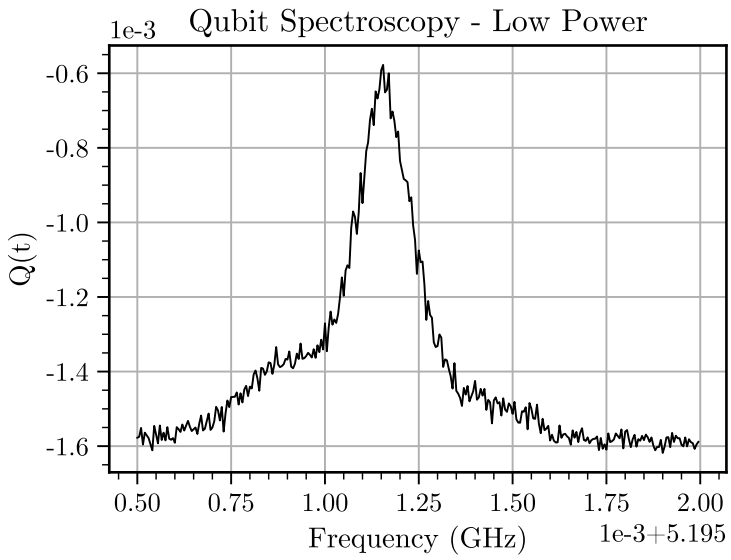


Figure 3.3: $\omega_{01}$ transition becomes sharper at lower input power due to reduced power broadening, limited by the intrinsic line width of the qubit. As can be seen, the qubit displays some charge dispersion and may lead to a TLS system later. [5]

At this stage, we have successfully characterized the qubit's frequency, resonator frequency and verified that both are functional. The next step is to measure the dynamics of the qubit using time-domain measurements.

## 3.2 Time-Domain Measurements

We proceed with time-domain measurements following the same order as outlined in Section (2.6). All the time domain-measurements shown below are done based on projective measurements, i.e. the qubit is found either in $|e\rangle$ or in $|g\rangle$. Hence, an ensemble measurement is done for each experiment below, where each data point is taken multiple times and averaged such that it converges to the probability of the qubit being in $|e\rangle$ or $|g\rangle$. Before each pulse sequence and subsequent measurement, the qubit is left undisturbed for a time of 1ms ($\gg T_1$) such that the qubit relaxes to the ground state ( corresponding to the thermal equilibrium of $\hbar\omega_0 \gg k_B T$) by losing energy to the environment.

### 3.2.1 Rabi Measurement

The initial measurement performed is a Rabi experiment, utilizing a minimal input power to the qubit. At this step, readout power is manually optimized to be max-

imum possible value such that the qubit does not get overwhelmed ('punch-out') for the best SNR. The $I(t)$ and $Q(t)$ data streams received from the demodulation mixer are rotated digitally to get all data in $Q(t)$. Further, the data is rotated by $(n * \pi)$ such that $Q(t)$ corresponding to the ground state is lower than the excited state for visual clarity.

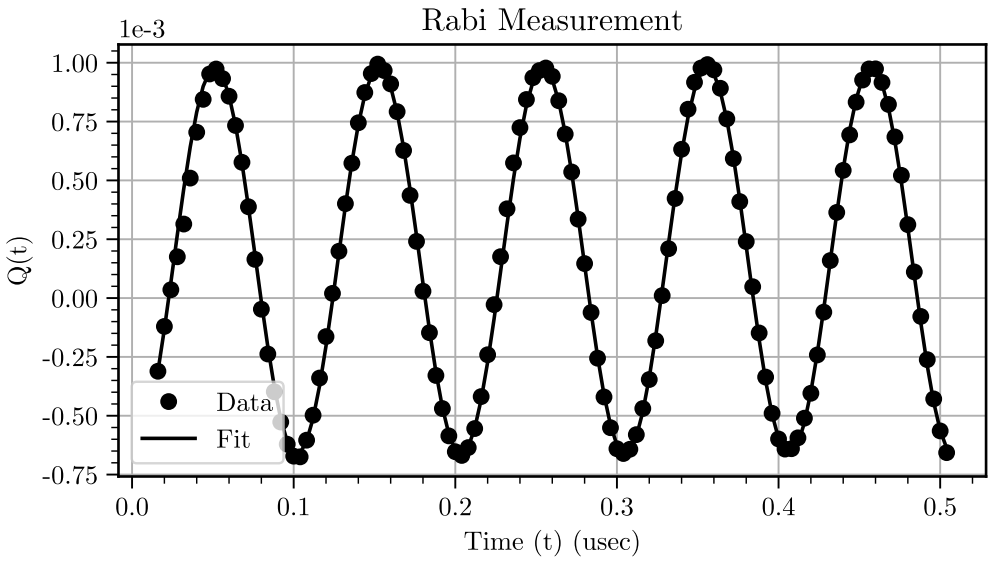


Figure 3.4: For the Rabi Experiment, a pulse of time 't' is applied on the qubit and measured. As expected a sine curve is obtained.

In the data shown, the qubit essentially traverses on a circle on the Bloch sphere (refer Figure 1.2). Corresponding to a projection on the measurement axis, we obtain a sine curve (Figure 3.4). The data is fit to a sine curve to obtain the Rabi frequency as 9.847MHz. The Rabi frequency ($\Omega_R$) depends on how hard the qubit is driven ($\Omega_d$) and the detuning of the drive from the qubit ($\Delta_d$):

$$\Omega_R = \sqrt{\Omega_d^2 + \Delta_d^2}$$

In this case, we used 0.1 of the max amplitude (at control) available at the AWG. We adjust the readout pulse amplitude at this stage for the maximum separation between the $|0\rangle$ and $|1\rangle$ states as seen after demodulation in $I(t)$ and $Q(t)$. Since the excited and ground state values are known, further experiments can be normalized against this curve to obtain the probability of the qubit being in $|e\rangle$. Further, we adjust the angle of rotation such that all relevant data is contained in one of the channels. The next step is to calibrate standard pulses, such that we can prepare the qubit in desired states.

### 3.2.2 Power Rabi Measurement

We calibrate $\pi/2$ pulses using the power rabi experiment (refer section 2.6). We fix our $\pi/2$ pulse length as 175ns. The reason for this choice is the relatively low power-output in the super-heterodyne setup (refer figure 3.12). Since this renders the amplitude used in the AWG to be very low, we attach a 10dB attenuator between the control port at the OPX and the mixer in figure (2.3). We start by sending $N = 2$, $\pi/2$ pulses to the qubit:

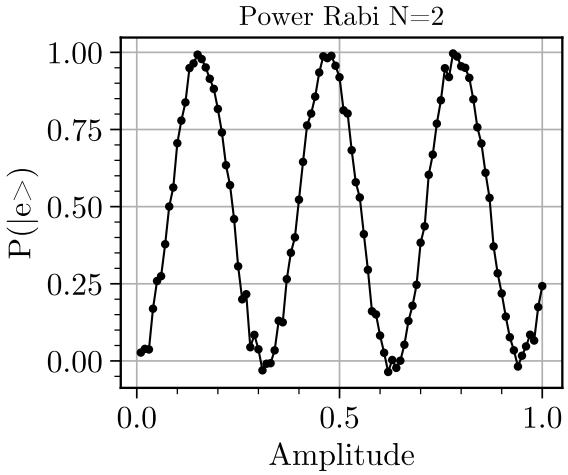


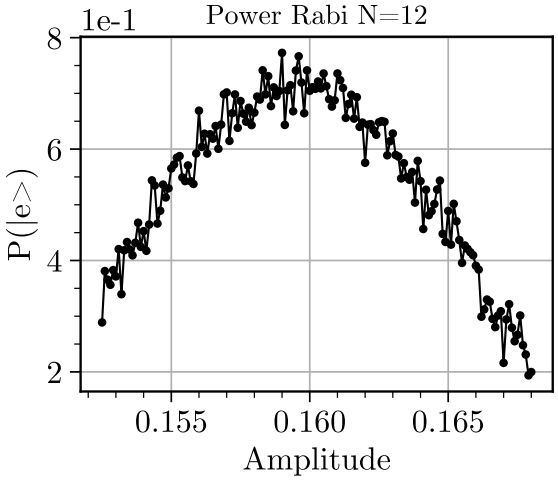


The first peak corresponds to the amplitude where two cascaded $\pi/2$ pulses of length 175ns excite the qubit to the $|e\rangle$ state. We can therefore use the amplitude

corresponding to the peak. In practice, we increase our sampling around the peak and increase the number of pulses iteratively until desired accuracy in amplitude is achieved.
The pulse amplitude for $\pi/2$ pulses we extract is 0.159. This precision is sufficient for our next experiments, however, we will refine this calibration later in section (3.4).

### 3.2.3 Ramsey Measurement

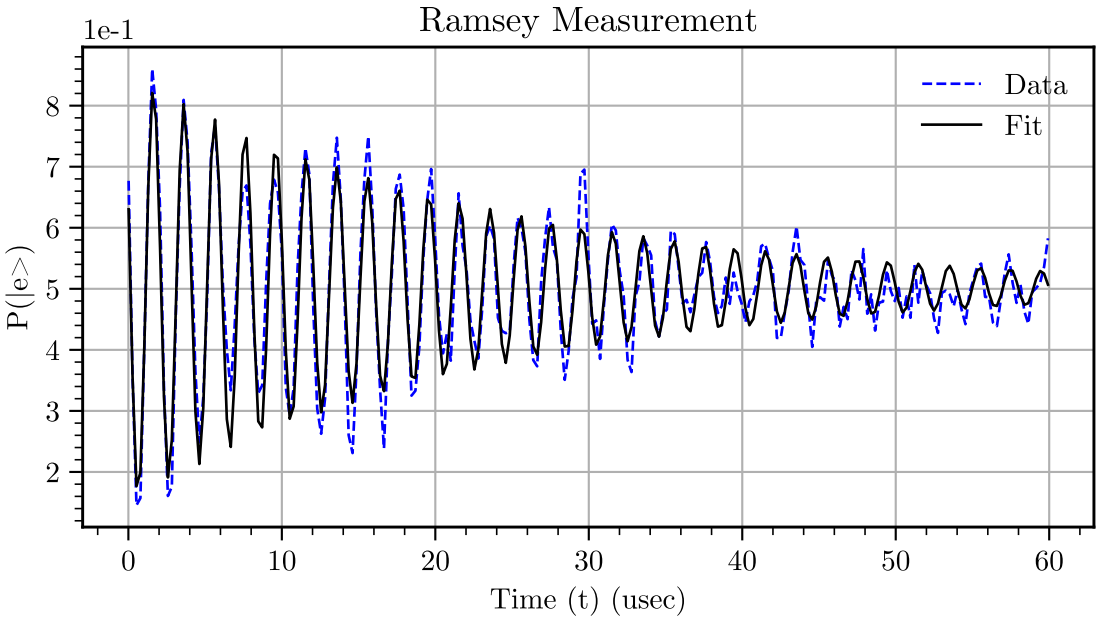


Figure 3.5: The Ramsey curve was obtained for a detuning $\Delta_d = 0.5$MHz. There is a presence of two frequencies in the 'Data' curve, due to charge dispersion discussed in figure (3.3). Therefore, beating is observed. This may affect our coherence times.

With a $\pi/2$ pulse calibrated, we can proceed to a Ramsey Experiment where we will ascertain the frequency of the qubit upto few tens of kilo-hertz. A detuning of 0.5 MHz is purposefully set up and the data obtained is shown in figure (3.5). The data is fit to equation (2.4). The detuning we obtain from the fit is $0.511 \pm 0.004$MHz. Hence, we can correct for the extra detuning (than the expected) of 0.011MHz. Therefore, we set our control pulses at a frequency of 5.196111GHz. We are able to ascertain the qubit frequency within few tens of kilo-hertz and can now proceed to measure the coherence times of the qubit.

### 3.2.4 Coherence Measurement

The coherence experiment aims to measure the relaxation and dephasing dynamics of the qubit, i.e., $T_1$ measurement from a relaxation time experiment, $T_2^*$ from Ramsey experiment and $T_2$ from Hanh echo experiment are extracted. We obtain the following results:

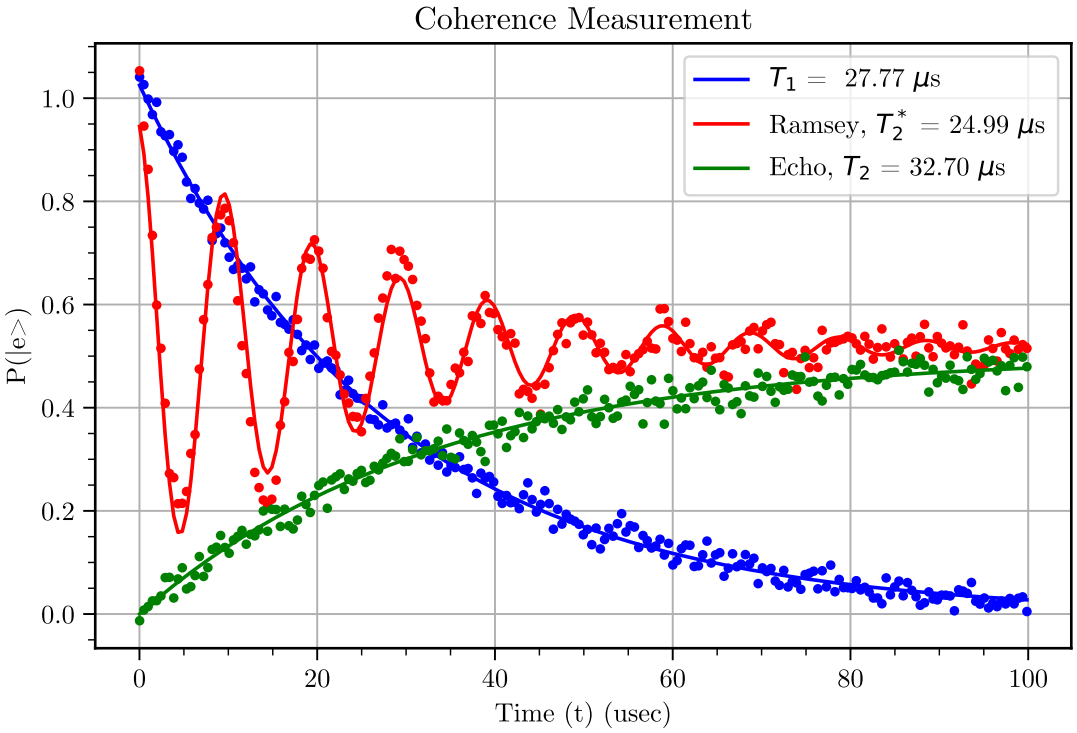


Figure 3.6: (color) A coherence dataset. As expected, Ramsey ($\Delta_d = 0.1$MHz) begins with the excited state, and decays to the mixed state. Echo curve begins from the ground state and decays to the mixed state. T1 curve begins from the excited state and decays to the ground state.

The coherence times of the qubit are obtained as:

- $T_1 = 27.77 \pm 0.34 \mu$sec
- $T_2^* = 24.99 \pm 1.05 \mu$sec
- $T_2 = 32.7 \pm 1.09 \mu$sec

## 3.3 Measurements from the Super-heterodyne setup

The super-heterodyne setup can now be used to control the qubit. Given qubit characteristics from the standard setup have been measured, we can proceed to test our new scheme. We begin by going through the filter fabrication.

### 3.3.1 Filter setup

The filter requirements are decided based on the mixer and frequencies chosen. In our experiments, we observed that the mixer we employed had a high conversion loss when operated at high IF frequencies. Therefore, we used a reasonable IF frequency of 2.5GHz. This frequency was found to be large enough to keep the filtering requirements reasonable. Since our aim was to test qubit control, the lower side band must be between 4-5.5GHz. Therefore, the LO would range between 6.5GHz to 8 GHz and the upper side band would range from 9GHz to 10.5GHz.

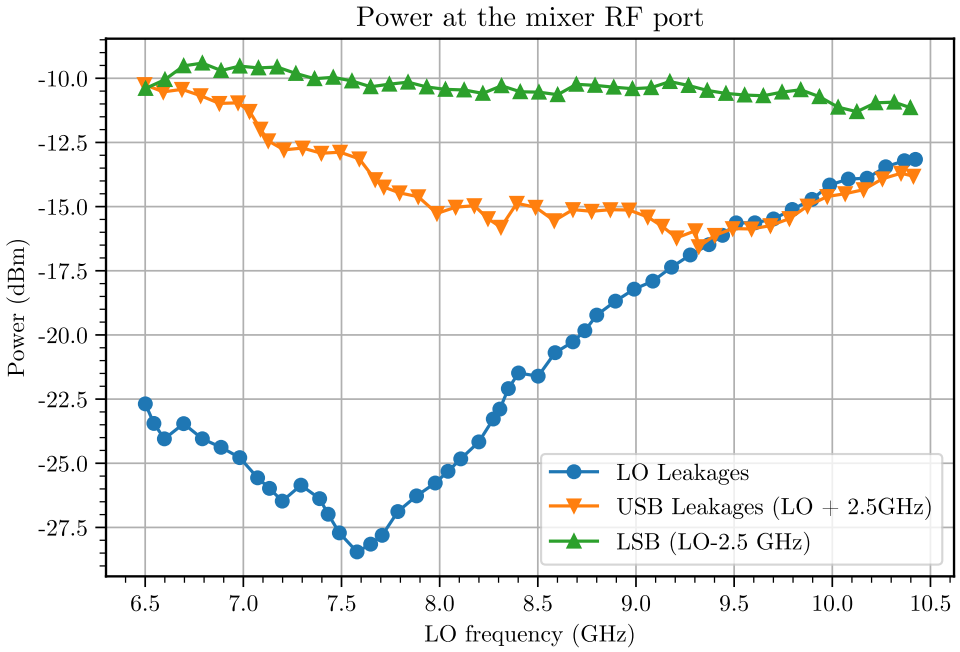


Figure 3.7: RF output powers from the mixer measured by the spectrum analyzer. Lower side band (LSB) is the desired band. Upper side band (USB) and LO are treated as leakages and must be suppressed. The input IF is fixed at 2.5GHz with power of 4dBm and input LO power is fixed at 15dBm, well within the ratings of the mixer.

As illlustrated in figure (3.7),a filter is necessary in order to suppress both the LO leakage and USB leakage. The filter must have a high attentuation for higher

frequencies. Additionally, it is imperative that the filter also suppress IF leakage at 2.5GHz. In light of these requirements, a sharp band-pass filter with 3dB points at 4GHz and 5.5GHz is deemed suitable for the given application.

An edge-coupled band-pass filter as described in Pozar's "Microwave Engineering" [7] is selected for implementation. The advantage of this type of filter lies in its ability to control impedance ranges, as well as its ease of manufacture without the need for vias. The working principle of this band-pass filter is based on the fact that in a coupled $\theta$ length transmission line, the impedance is given as [7]:

$$Z_{inp} = \frac{\sqrt{(Z_{0e} - Z_{0o})^2 - (Z_{0e} + Z_{0o})^2 \cos^2\theta}}{2\sin\theta} \tag{3.1}$$

i.e., the input impedance of such a filter is minimized at a certain frequency, $f_o$, where the electrical length, $\theta$, is equal to $\pi/2$. This corresponds to a $\lambda/4$ line, and the filter functions as a band-pass filter for frequencies in close proximity to $f_o$. By utilizing multiple sections of $\lambda/4$ lines, a filter with a high slope fall-off can be achieved. The number of sections used in the design is known as the order of the filter.

We utilize Cadence AWR software's *iFilter wizard* to design a 7th order Chebyshev band-pass filter. The substrate chosen for this design is *Rogers* FR4 board, characterized by a dielectric constant of 4 and a dielectric thickness of 1620$\mu$m. The selection of this substrate is done based on its sturdiness and low dielectric constant, which facilitated the use of the LPKF board prototyping mill for the physical realization of the filter design, with available reliable precision of up to 200$\mu$m. The measurements of the filter are described in detail in the appendix (A.1).

The response of the filter was verified before the fabrication with finite element simulations using Cadence AWR software, which agreed with the design. Upon testing after fabrication, the filter had a narrower pass band (figure 3.9). However, for our qubit, this filter can be used.

### 3.3.2 Power Stability

During the evaluation of the super-heterodyne setup, fluctuations in the power output were observed, preventing the successful calibration of $\pi$ and $\pi/2$ pulses. In order to determine the source of these fluctuations, a measurement of the power input into the system was conducted using a 13dB coupler attached at the end of the RF chain, in conjunction with a spectrum analyzer set in zero-span mode. By playing 500ns pulses through the RF chain system, the power being input to the fridge was measured.

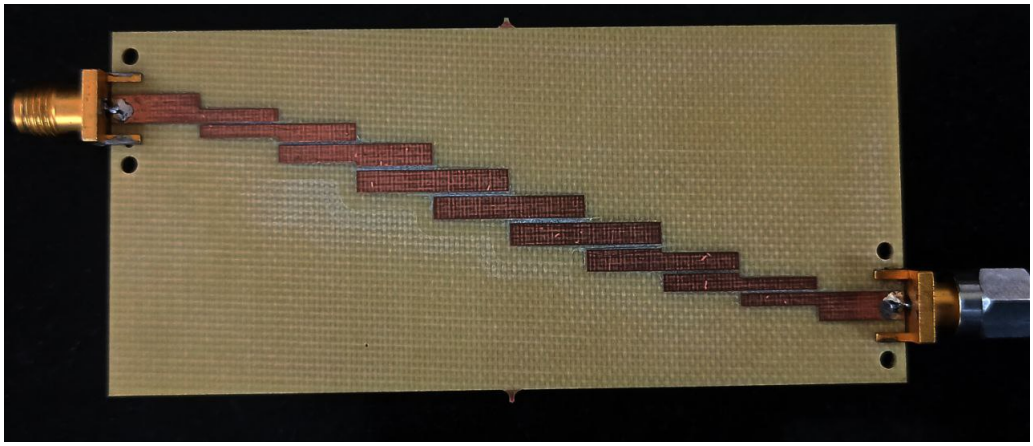

Figure 3.8: A 7th order edge coupled-line Chebyshev band-pass filter milled on an FR4 dielectric board. SMA connectors are attached on either side for ease of use.

Through a process of elimination, the source of the fluctuations in the RF chain had to be determined. Various combinations of components were tested, with the relevant data presented in Figure (3.10). It was found that the designed super-heterodyne configuration, which included an amplifier and a filter, exhibited power fluctuations of $\pm$1dBm. However, when the filter was removed and only the amplifier was utilized, the fluctuations were reduced to $\pm$0.4dBm. This observation suggests that the filter was the primary source of the fluctuations.

Given that the open filter is particularly susceptible to stray fields, a Faraday cage was constructed using thick aluminum sheet and aluminum tape. The power output of the amplifier and filter within the cage was subsequently measured, resulting in a significant reduction of the power fluctuations. Minimizing 5GHz radiation by turning off nearby Wi-Fi was also tried, where the ambient RF power due to the Wi-Fi routers was measured to be $-$40dBm. However, the Wi-Fi (5GHz) did not make a discernible difference on the power stability.

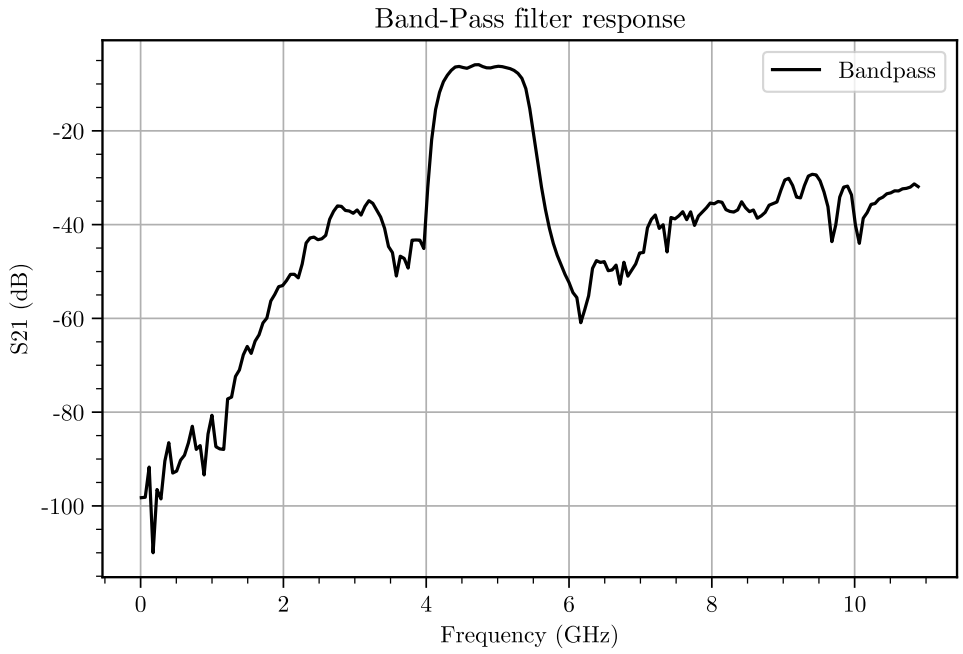


Figure 3.9: Transmission of the Band-Pass filter as measured experimentally. The filter has a loss of 7dB in the pass-band due to the di-electric material being lossy. The qubit frequency of 5.196GHz lies in the pass-band.

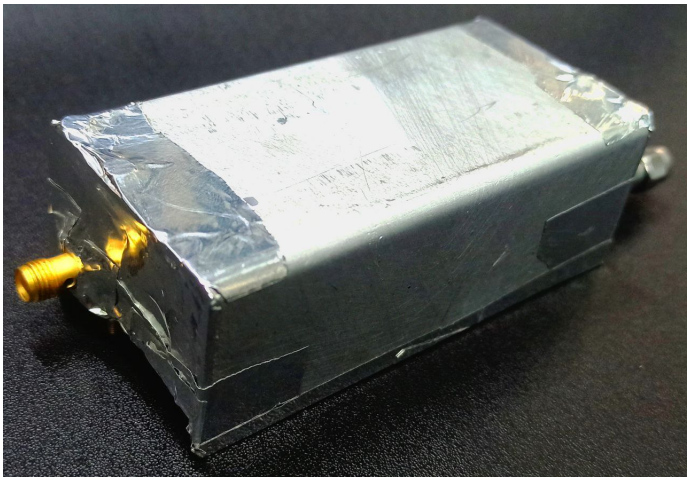

Figure 3.11: The filter was caged with a thick aluminum sheet and aluminum tape.

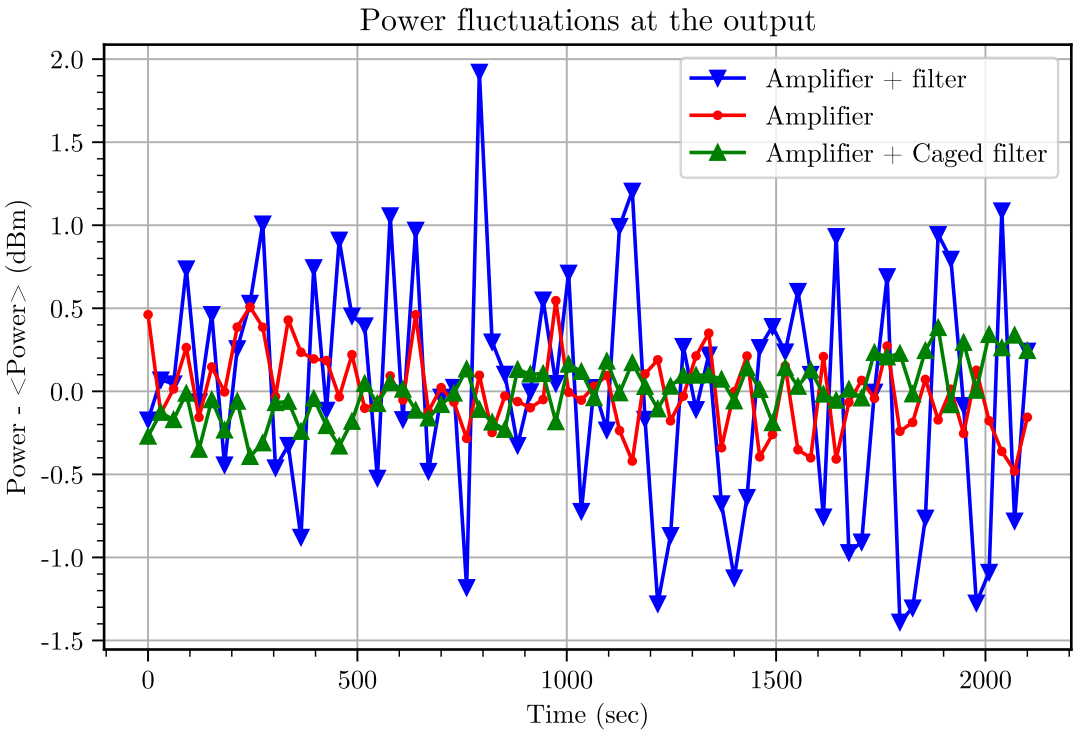


Figure 3.10: The fluctuations of the measured power at the spectrum analyzer coupled to the fridge input line using a 13dB directional coupler.

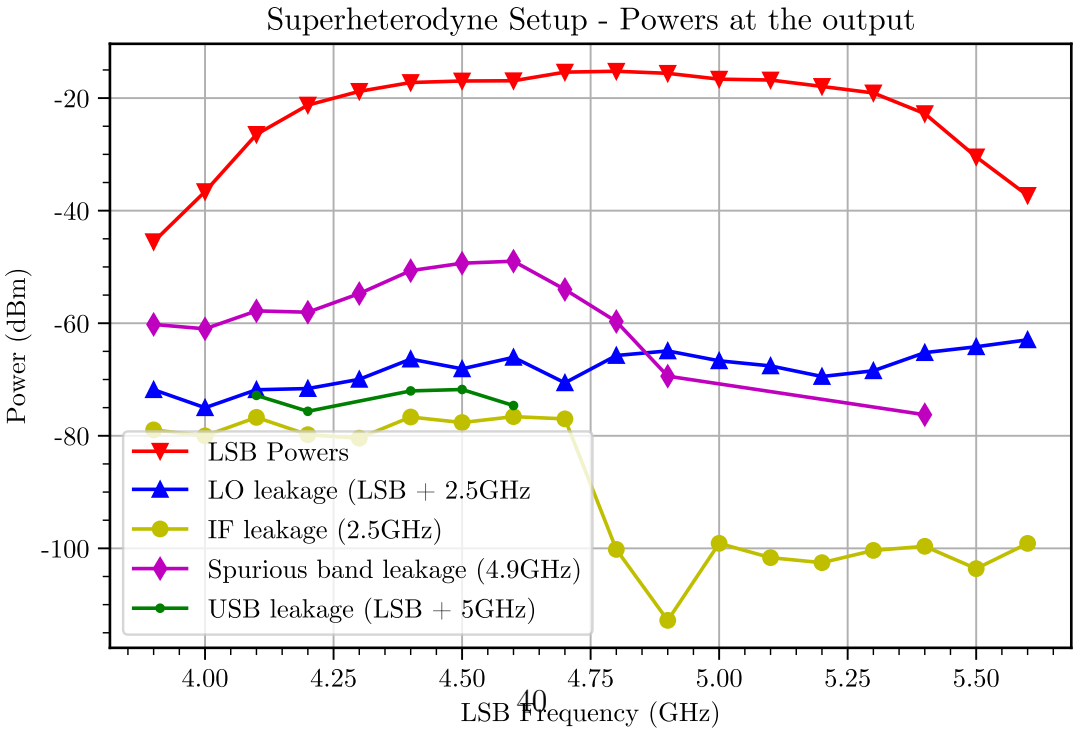




Figure 3.12: The leakages and powers obtained after the super-heterodyne setup on the spectrum analyser. The IF (2.5GHz) was set at 4dBm, and LO was set at 15dBm power. We observe a spurious free dynamic range of 40dBm. Similar implementations have reported upto 70dBm spurious free dynamic range [13], [14].

## 3.4 Stability Measurements - Bang-Bang

After troubleshooting power stability, we were able to calibrate the super-heterodyne setup and perform the Bang-Bang experiment. This experiment was repeated every 20 minutes, to capture any drifts and system instabilities with time. A raw data point is presented below for completeness.

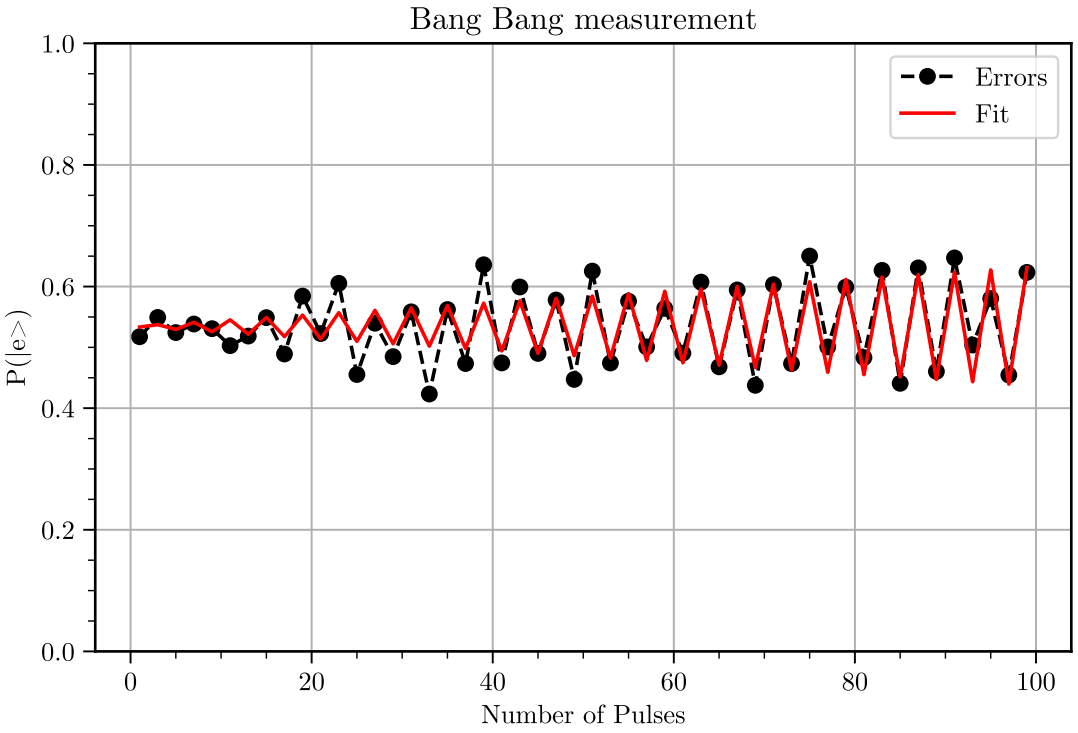


Figure 3.13: An example of a Bang Bang measurement taken using the standard OPX setup (2.3) at 13hrs 12min on 11-01-2023.

The results presented in figure (3.13) demonstrate the amplification of error as the number of pulses applied to the qubit increases. The data obtained from the experiment was fitted to the equation (2.7), from which the error was extracted to be $\epsilon = 0.00098 \pm 0.00007$. This error can be interpreted as the deviation of the projection on the z-axis upon measurement. In an ideal scenario, where the qubit is in an equal superposition state, the error would be equal to zero.

To further investigate the stability of the Bang-Bang measurements, we conducted multiple overnight experiments, the results of which are presented in figure (3.14). The first setup tested was the OPX standard setup (2.3), which involves SSB in IQ mixers. As depicted in the figure, the Bang-Bang measurements were

found to be highly stable over time. The second setup tested was the super-heterodyne setup, which exhibited a significant degree of fluctuations over time.

The fluctuations observed in the super-heterodyne setup could be attributed to a variety of factors. To identify the source of these fluctuations, a systematic examination of different components was conducted. This included testing different amplifiers and their combinations, however, these changes did not result in an improvement of the setup. Additionally, the amplifiers were found to be operating within their linear regime. The fluctuations did not appear to follow any clear trend, ruling out the possibility of slow temperature fluctuations as the cause.

Through a process of elimination, the suspected component was identified as the filter. To further investigate this, the OPX standard setup, which had performed well without any fluctuations, was examined.

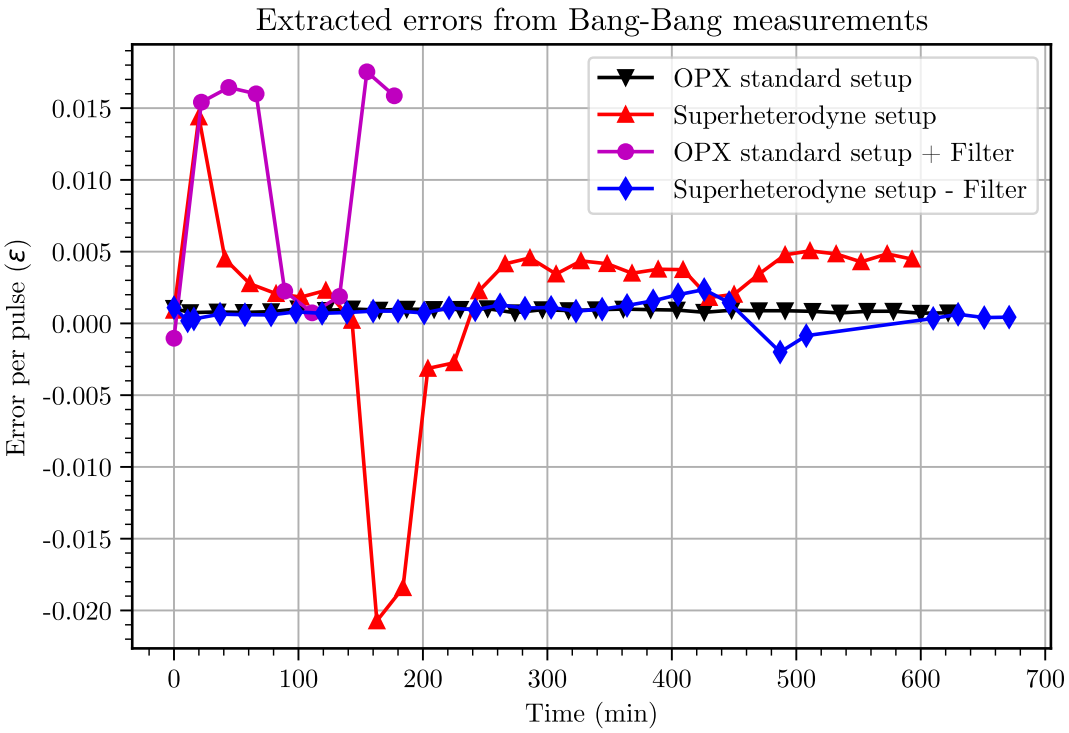


Figure 3.14: Errors with time extracted from Bang-Bang measurements over time. Multiple combinations of the setups were tested as shown.

However, in this iteration, the super-heterodyne filter was attached to the OPX setup. It was expected that this would not affect the control line, as the filter was designed specifically for qubit control. However, it was quickly determined (based on the short dataset taken) that the fluctuations arose as a result of the filter. This

suggests that the filter employed in the super-heterodyne setup is the contributing factor to the observed fluctuations.

Since the IF frequency in the super-heterodyne setup is large (2.5GHz), the LO and USB frequencies are very far away from the qubit frequencies. While it is not ideal, the super-heterodyne setup was tested without any filters. In this case, the fluctuations died down and the result was similar to the standard OPX setup. This suggests the fact that the only component adding to fluctuations in the setup is the custom filter.

# Chapter 4

# Concluding Remarks

In this thesis, we successfully probed and manipulated a superconducting transmon qubit. Through frequency spectroscopy, we determined the frequencies of both the cavity and the qubit. We employed a "punch-out" experiment to check if the qubit was functional. Subsequently, we observed Rabi oscillations and excited the qubit over a range of different timescales, which allowed us to calibrate the $\pi$ and $\pi/2$ pulses that serve as the fundamental building blocks of qubit control. Further, we performed a Ramsey interferometry experiment, which enabled us to accurately ascertain the qubit frequency to within a few kilohertz. Finally, we conducted a detailed characterization of the transmon's coherence lifetimes.

We have presented an alternative approach for the control of superconducting qubits utilizing double frequency up-conversion (also known as super-heterodyning). Our results indicate that this method is capable of achieving stability for prolonged periods of time, comparable to that of standard techniques. Additionally, by leveraging this method, we were able to expand the accessible frequency range and simplify the required RF components. This approach eliminates the need for two separate $I(t)$ and $Q(t)$ channels, enabling a more efficient use of microwave RF components.

**Possible Improvements:**
It is important to note that there are potential avenues for further improvement in the setup we have implemented. Specifically, the pulse duration of $\pi/2$ pulses we have used is relatively high at 175ns, against the typical range of tens of nanoseconds. The solution to this issue would be the incorporation of an additional stage of amplification in order to reduce pulse duration. Additionally, the filter used in our setup was found to be a source of power fluctuations. By exploring alternative band-pass filter designs, and implementing shielding measures to protect against stray fields, we believe it would be possible to mitigate this issue and improve the overall performance of the system. By utilizing higher-quality low-loss dielectrics

such as TMM6 or TMM10 in the fabrication process, rather than the currently used lossy medium FR4, it is likely that we could achieve low losses and fluctuations. Further, the filter can be designed to have a broader pass band to allow for more range. The IF frequency can be increased from 2.5GHz to about 6GHz to achieve isolation from any unwanted signals near the readout and qubit frequencies. Finally, this system can be standardized with the first stage being fixed from system to system.

**Future Avenues:**
In the last two years, emergence of 5G technologies has led to the development of advanced field-programmable gate array (FPGA) boards that feature digital-to-analog converters (DACs) with increased sampling rates, such as the RFSoC board utilized in our super-heterodyne setup. This technology has the potential to enable the direct generation of qubit control tones from the DAC, and by utilizing multi-nyquist zones, it is possible to create tones that exceed the standard sampling rate of the DAC. Furthermore, these boards are equipped with analog-to-digital converters (ADCs), which allows for the implementation of sub-nanosecond qubit readout and the execution of conditional operations on the qubits. Some reports as in the literature (Stefanazzi et al., 2021) [15], have already demonstrated the feasibility of this approach in the context of superconducting qubits control and measurement.

# Appendix A

## A.1 Band-pass filter dimensions

The filter is chosen to be an impedance controlled band-pass filter. We choose the FR4 board with a di-electric of 4 of thickness 1620$\mu$m as our substrate. The substrate was chosen for its ease of availability, cost and most of all larger design dimensions which were easy to fabricate. The frequency of the pass-band was tuned to be 4.85GHz instead of the accepted geometric mean of the two 3dB points, after simulating transmission responses in Cadence AWR using finite element methods. The dimensions of the designed filter are presented below:

```
Physical Model
Dimensions:  78547.1um x 28323.2um
Area:  2.2247e+06um
Layout grid size:  5000um
Technology:  Microstrip (H=1620um, Er=4, T=35um, Hu=0um)
Parts
TLN: W=3309.9um, L=4427.4um
STEP: W1=3309.9um, W2=1216.5um, Offset=-1046um
PCL: W=1216.5um, S=213.22um, L=8900.0um
STEP: W1=1216.5um, W2=2025.5um, Offset=-404.4um
PCL: W=2025.5um, S=283.02um, L=8727.2um
STEP: W1=2025.5um, W2=2446.1um, Offset=-210.2um
PCL: W=2446.1um, S=416.12um, L=8623.0um
STEP: W1=2446.1um, W2=2545.5um, Offset=-49.72um
PCL: W=2545.5um, S=467.43um, L=8595.7um
PCL: W=2545.5um, S=467.43um, L=8595.7um
STEP: W1=2545.5um, W2=2446.1um, Offset=-49.72um
PCL: W=2446.1um, S=416.12um, L=8623.0um
STEP: W1=2446.1um, W2=2025.5um, Offset=-210.2um
PCL: W=2025.5um, S=283.02um, L=8727.2um
```

```
STEP: W1=2025.5um, W2=1216.5um, Offset=-404.4um
PCL: W=1216.5um, S=213.22um, L=8900.0um
STEP: W1=1216.5um, W2=3309.9um, Offset=-1046um
TLN: W=3309.9um, L=4427.4um
```

As expected the filter is symmetrical. The design begins and ends (TLN above) from a 50Ω launch.

# References


[1] Michael A. Nielsen and Isaac L. Chuang. *Quantum computation and quantum information*. 10th anniversary ed. Cambridge ; New York: Cambridge University Press, 2010. ISBN: 9781107002173.

[2] P. Krantz et al. *A quantum engineer's guide to superconducting qubits*. en. June 2019. DOI: 10.1063/1.5089550. URL: https://aip.scitation.org/doi/abs/10.1063/1.5089550.

[3] M. H. Devoret, A. Wallraff, and J. M. Martinis. *Superconducting Qubits: A Short Review*. arXiv:cond-mat/0411174. Nov. 2004. URL: http://arxiv.org/abs/cond-mat/0411174.

[4] Mahdi Naghiloo. *Introduction to Experimental Quantum Measurement Superconducting Qubits*. Apr. 2019. arXiv: 1904.09291 [quant-ph].

[5] Jens Koch et al. "Charge-Insensitive Qubit Design Derived from the Cooper Pair Box". In: *Physical Review A* 76.4 (Oct. 12, 2007), p. 042319. ISSN: 1050-2947, 1094-1622. DOI: 10.1103/PhysRevA.76.042319. URL: https://link.aps.org/doi/10.1103/PhysRevA.76.042319.

[6] E T Jaynes and F W Cummings. "Comparison of quantum and semiclassical radiation theories with application to the beam maser". In: *Proc. IEEE Inst. Electr. Electron. Eng.* 51.1 (1963), pp. 89–109.

[7] David M. Pozar. *Microwave engineering*. 4th ed. OCLC: ocn714728044. Hoboken, NJ: Wiley, 2012. ISBN: 9780470631553.

[8] G. J. Dolan. "Offset masks for lift-off photoprocessing". en. In: *Applied Physics Letters* 31.5 (Sept. 1977), pp. 337–339. ISSN: 0003-6951, 1077-3118. DOI: 10.1063/1.89690. URL: http://aip.scitation.org/doi/10.1063/1.89690 (visited on 01/11/2023).

[9] Sumeru Hazra. *Enhancing qubit connectivity in superconducting quantum processors*. Tata Institute of Fundamental Research, 2022.

[10] R. Vijay, M. H. Devoret, and I. Siddiqi. "Invited Review Article: The Josephson bifurcation amplifier". en. In: *Review of Scientific Instruments* 80.11 (Nov. 2009), p. 111101. ISSN: 0034-6748, 1089-7623. DOI: 10.1063/1.3224703. URL: http://aip.scitation.org/doi/10.1063/1.3224703 (visited on 01/23/2023).

[11] David Reed. *Entanglement and Quantum Error Correction with Superconducting Qubits*. Yale University, 2013.

[12] Sarah Sheldon et al. "Characterizing errors on qubit operations via iterative randomized benchmarking". en. In: *Physical Review A* 93.1 (Jan. 2016), p. 012301. ISSN: 2469-9926, 2469-9934. DOI: 10.1103/PhysRevA.93.012301. URL: https://link.aps.org/doi/10.1103/PhysRevA.93.012301 (visited on 01/17/2023).

[13] Johannes Herrmann et al. "Frequency Up-Conversion Schemes for Controlling Superconducting Qubits". In: (2022). DOI: 10.48550/ARXIV.2210.02513. URL: https://arxiv.org/abs/2210.02513 (visited on 01/17/2023).

[14] Jonathan Dearlove, Prasanna Pakkiam, and Arkady Fedorov. "Double Upconversion for Superconducting Qubit Control realised using Microstrip Filters". In: (2022). DOI: 10.48550/ARXIV.2210.09498. URL: https://arxiv.org/abs/2210.09498 (visited on 01/17/2023).

[15] Leandro Stefanazzi et al. "The QICK (Quantum Instrumentation Control Kit): Readout and control for qubits and detectors". In: (2021). DOI: 10.48550/ARXIV.2110.00557. URL: https://arxiv.org/abs/2110.00557 (visited on 01/17/2023).